Zaera, R.; Rodríguez-Martínez, J.A.; Vadillo, G.; Fernández-Sáez, J.; Molinari, A. (2015). Collective behaviour and spacing of necks in ductile plates subjected to dynamic biaxial loading. *Journal of the Mechanics and Physics of Solids*. Vol., pp. 245-269.

DOI: https://doi.org/10.1016/j.jmps.2015.09.001

Collective behaviour and spacing of necks in ductile plates subjected to dynamic biaxial loading

R. Zaera[a], J.A. Rodríguez-Martínez[a,b], G. Vadillo[a], J. Fernández-Sáez[a], A. Molinari[b,*]

[a] *Department of Continuum Mechanics and Structural Analysis. University Carlos III of Madrid. Avda. de la Universidad, 30. 28911 Leganés, Madrid, Spain*

[b] *Laboratoire d'Etudes des Microstructures et de Mécanique des Matériaux LEM3, UMR CNRS 7239, Université de Lorraine, Ile du Saulcy, 57045 Metz cedex 1,France*

Abstract

Diffuse or localized dynamic necking of a sheet metal is a major issue in high speed forming processes, leading to unacceptable thinning and even failure if fully developed, and in the dynamic behaviour of metallic structural elements of small thickness used for energy absorption purposes. This process is frequently related to the collective development of localization bands resulting in a necking pattern which depends on the sheet properties and on the loading conditions. This work investigates the spacing between necking bands in sheets made of a thermoviscoplastic metal and submitted to dynamic biaxial loading. For that task a linear perturbation technique, derived within a 2D framework which specifically accounts for stress triaxiality effects upon strain localization, has been developed. Using this methodology, a dominant instability mode can be identified, whose wavelength is related to the necking-band spacing. Likewise, fully 3D finite element simulations have been performed in order to verify and complement the outcomes of the aforementioned theoretical approach. The effects of loading conditions (loading path and loading rate), and thermal coupling on the stability of the deformation process and on the distance between necking bands are examined. We have shown that the neck spacing increases with the ratio of strains and decreases with the loading rate and the temperature rise.

Keywords:

Dynamic biaxial loading, Linear stability analysis, Finite element simulations, Necking bands spacing, Inertia

*Corresponding author. Tel. +33 387315369; Fax: +33 387315366. E-mail address: alain.molinari@univ-lorraine.fr

Nomenclature

1. Introduction

Sheet metal forming is devised to make products of complicated shapes which are widely used in, for instance, aeronautical and automotive industries. The success of this type of metal-working processes is determined by the maximum deformation that the material can withstand, which is closely tied to the onset of plastic instabilities like shear bands and necking. Regarding the sheet necking phenomena, two stages in the instability process are usually identified: the diffuse necking (Swift, 1952) and the localized necking (Hill, 1952). A useful tool to design and optimize metal forming processes is the forming limit diagram (FLD). $FLDs$ show the combination of major and minor in-plane principal strains prior to the onset of localized necking. The concept, originally introduced by Keeler and Backofen (1963), was fully developed by Goodwin (1968).

In order to obtain theoretical $FLDs$, the localized necking model proposed by Hill (1952) could be used. However, within the framework of the flow plasticity theory, this procedure predicts an infinite ductility under stretching conditions when the ratio of strains (major to minor in principal strains) is positive, while experiments show that necking appears in biaxially stretched sheets. To allow for necking inception, Marciniak and Kuckzynski (1967) introduced imperfections (caused by factors such as local grain variation, texture, thickness reduction,...) normal to the axis of maximum principal strain. An alternative approach to resolve the discrepancy observed with the Hill's model was proposed by Stören and Rice (1975), who performed a study based on bifurcation analysis using a J_2 rate-independent deformation theory, which introduced an effect similar to a pointed vertex on the yield loci, promoting instability in biaxial tension. This procedure has been further reformulated by several authors (Hutchinson et al., 1978; Needleman and Rice, 1978; Chin-Chan, 1995; Novak and Laurova, 1989; Zhu et al., 2001).

The linear perturbation analysis is an alternative approach to analyze the problem (Dudzinski and Molinari, 1988, 1991; Toth et al., 1996; Li and Chandra, 1999; Li et al., 2012). The method consists on superimposing a perturbation to the basic homogeneous

Symbol	Definition
t	Time
η	Perturbation growth rate
$\boldsymbol{e}$	Effective e-instability
X,Y,Z	Lagrangian coordinates of principal strain rate directions
x,y,z	Eulerian coordinates of principal strain rate directions
X_1,X_2	Lagrangian coordinates of perturbation directions
x_1,x_2	Eulerian coordinates of perturbation directions
Ψ	Angle between directions X and X_1
L_x,L_y	Dimensions of the sheet in directions X,Y
h	Sheet thickness
$2a$	Neck thickness
ϕ	Bridgman's correction factor
ξ	Perturbation wavenumber
U_x,U_y	Displacements in directions X,Y (lagrangian description)
V_x,V_y	Velocities in directions X,Y (lagrangian description)
v_x,v_y	Velocities in directions X,Y (eulerian description)
A_x,A_y	Accelerations in directions X,Y (lagrangian description)
ε_x,ε_y,ε_z	Logarithmic strains in directions X,Y,Z
χ_ε	Ratio of strains in directions Y and X
$\chi_{\dot{\varepsilon}}$	Ratio of strain rates in directions Y and X
$\bar{\varepsilon}$	Equivalent strain
$\boldsymbol{F}$	Deformation gradient tensor
$\boldsymbol{d}$	Rate of deformation tensor
$\boldsymbol{l}$	Velocity gradient tensor
$\boldsymbol{\sigma}$	Cauchy stress tensor
$\boldsymbol{\sigma}^{neck}$	Stress across the neck
$\boldsymbol{\sigma}^{avg}$	Uniform stress across the neck
$\boldsymbol{\sigma}^{u}$	Averaged stress across the neck
$\bar{\sigma}$	Equivalent stress
σ_Y	Yield stress
κ	Plastic multiplier

Table 1: *Symbols 1.*

Symbol	Definition
θ	Temperature
ρ	Mass density
σ_{yo}	Reference yield stress
$\dot{\bar{\varepsilon}}_{ref}$	Reference strain rate
n	Strain hardening coefficient
m	Strain rate hardening coefficient
ν	Temperature softening coefficient
β	Taylor-Quinney coefficient
k	Thermal conductivity
c	Heat capacity per unit volume
$\dot{\square}$	Material time derivative
$\hat{\square}$	Non-dimensional variable
$\square^0$	Variable at time $t = 0$
$\square^1$	Variable at perturbation time $t = t^1$
$\square^{\mathscr{L}}$	Variable in the material configuration
$\square^{\mathscr{E}}$	Variable in the spatial configuration
$\square_c$	Critical value of the variable (at maximum perturbation growth)

Table 2: *Symbols 2.*

flow at certain stage of the postulated homogeneous deformation process of the sheet. The flow instability or stability is established by the increasing or decreasing character of the perturbation. The method has been used in Solid Mechanics for the analysis of plastic localization under shear loading (Bai, 1982; Molinari, 1985; Molinari and Clifton, 1987; Rodríguez-Martínez et al., 2015a), uniaxial tensile loading (Fressengeas and Molinari, 1985; Zhou et al., 2006; Vadillo et al., 2012; Rodríguez-Martínez et al., 2013a,b, 2015b; Zaera et al., 2014) and plane strain conditions (Mercier and Molinari, 2003; Jouve, 2013a,b).

Several phenomenological ductile fracture criteria (Cockcroft and Latham, 1968; Oh et al., 1979; Oyane et al., 1980; Ko et al., 2007; Bai and Wierzbicki, 2010) have been used to predict the forming limit diagrams (Clift et al., 1990; Wifi et al., 1996; Takuda et al., 1999; Han and Kim, 2003; Ozturk and Lee, 2004; Liu et al., 2009; Chen et al., 2010). Lou et al. (2012) predicted the fracture forming limit diagrams of sheet metals using models based on nucleation, growth and coalescence of voids (Gurson, 1977; Tvergaard and Needleman, 1984). Continuum Damage Mechanics Approach (CDM) (Krajcinovic and Lemaitre, 1987; Lemaitre and Chaboche, 1990) is the base of other ductile damage criteria employed in this field (Lemaitre, 1993; Tai, 1985; Wang, 1995; Aboutalebi et al., 2012).

Since the strain rate affects both plastic flow and ductility of metals, its influence in forming limit diagrams could be expected. In this regard, theoretical research on the rate sensitivity of $FLDs$ (Hutchinson et al., 1978; Lee and Zaverl, 1982; Barata da Rocha et al., 1985; Graf and Hosford, 1990; Nie and Lee, 1991; Li and Chandra, 1999; Zhang et al., 2009; Li et al., 2012) as well as intensive experimental work (Percy, 1980; Shimamoto et al., 2003; Oliveira et al., 2005; Lee et al., 2008; Grolleau et al., 2008; Jie et al., 2009; Zhang et al., 2009; Ramezani and Ripin, 2010; Zidane et al., 2010; Verleysen et al., 2011) was conducted in the last decades. A large variety of strain rates can be achieved using different sheet metal forming processes. Thus, Shimamoto et al. (2003) performed tests on cruciform specimens of $AA7075-T6$ at 1 m/s, while Zidane et al. (2010) used an hydraulic machine applying a loading speed of 2 m/s. In the intermediate range of strain rate (100 s^{-1} to 500 s^{-1}), the works of Grolleau et al. (2008) and Ramezani and Ripin (2010) could be quoted. Using special forming techniques such as magnetic pulse forming (Oliveira et al., 2005) or explosive forming (Percy, 1980), high rates of deformation (up to 3500 s^{-1}) are found.

Some authors (Jie et al., 2009; Verleysen et al., 2011) pointed out that the effect of strain rate on $FLDs$ is non-negligible and strongly material dependent. Jie et al. (2009) showed the importance to consider the true rate dependency of the material for a correct prediction of the FLD experimentally obtained. On the other hand, depending on the material and operational conditions different trends have been observed. Thus, Lee et al. (2008) concluded that the forming limit diagram of $AZ31$ Mg alloy decreases with increasing strain rate. The $FLDs$ of the steels with low quasi-static ductility improves significantly at high strain rates, while this variable does not affect the forming limit of steels with already high quasi-static ductility (Seth et al., 2005). Verleysen et al. (2011) reported a downward shift in the FLD of the $S235$ and $DC04$ steel grades at high strain rates, and the opposite trend for the case of a $CMnAl$ $TRIP$ steel, while the strain rate does not have a significant effect on the $AISI$ 904. The reasons for such diverse responses observed could be related with the strong material dependency (strain hardening, strain rate sensitivity, temperature sensitivity), as well as with the interaction between different coupled effects present in the process (inertia, strain rate, loading path and geometrical effects).

In particular the inertial effect which plays a crucial role in dynamic deformation processes (Fressengeas and Molinari, 1985; Rodríguez-Martínez et al., 2013b) has not been clearly identified in the construction of $FLDs$. In fact, the different theoretical approaches pointed out before (Hill, 1952; Marciniak and Kuckzynski, 1967; Stören and Rice, 1975; Dudzinski and Molinari, 1991; Li et al., 2012) and others assume quasi-static conditions. Therefore, we present a theoretical approach to analyse the necking instability of a biaxially stretched sheet considering inertial effects. This problem can be considered as a model to study the formability of metals. Two complementary methodologies are used in our investigation: linear stability analysis and finite element simulations. The results obtained with the second method (necking strain, necking wavelength, necking orientation) at different strain rates, are rationalized with the first one, permitting to determine the conditions for the development of plastic instabilities in the sheet.

The paper is organized as follows. Section 2 is devoted to present the governing equations of the problem, together with the initial and boundary conditions. The third and fourth sections describe the linear stability methodology and the finite element modelling

of the problem at hand. Section 5 shows the salient features of the stability analysis, identifying the critical perturbation growth, the critical direction of perturbation and the critical wavenumber. Section 6 presents some key outcomes of this investigation, uncovering the effect of loading path, loading rate and thermal coupling on plastic flow localization, focusing our attention on the necking band spacing. The final conclusions of this investigation are given in section 7.

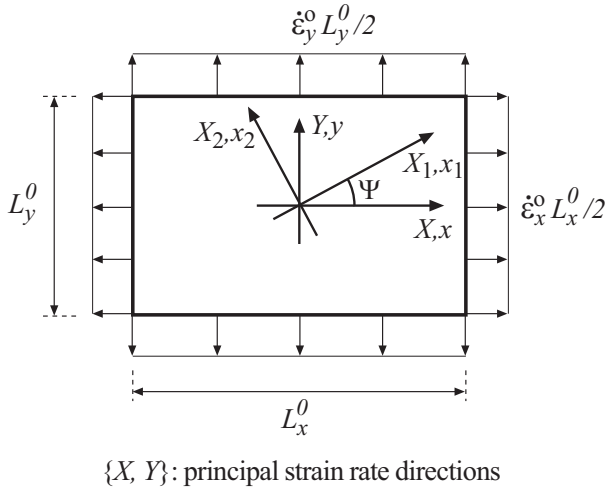

Figure 1: Axes of loading and of perturbation. The directions of the overall principal strain rate are x and y. The perturbation is constant on lines $X_1 = constant$.

2. Governing equations

From now on capital letters representing coordinates, displacements, velocities or accelerations will be used for the Lagrangian frame, and lowercase letters for the Eulerian frame. Let us consider a rectangular sheet of initial thickness h^0 and edges of initial lenght L_x^0 and L_y^0. The sheet is subjected to constant and opposed velocities on opposed sides, as shown in Fig. 1. Directions X and Y are therefore of overall principal strain rates (see Appendix A for details on the kinematics of the problem). It is supposed that this loading condition is always satisfied, thus elastic unloading is disregarded.

Under conditions of homogeneous deformation, the stress components are considered as uniform through the thickness of the sheet, and direction z is of plane stress. However, strain localization may lead to a stress gradient along thickness. Following the theory

developed by Bridgman for two-dimensional specimens, the present work accounts for this triaxiality effect on the stress in direction x_1 (perpendicular to the neck), permitting to calculate the averaged value of this stress along the thickness through the use of a correction factor depending on a geometric parameter (ratio of thickness to curvature radius of the neck). While Bridgman's theory considers either plane strain or plane stress conditions in a direction contained in the sheet, the authors validated it for a general case with arbitrary ratios of strain (see Appendix B for details).

The material is taken to be incompressible, of mass density ρ, with a mechanical behavior described by the Huber-Mises plasticity theory, and the yield stress is given by a simplified constitutive relation linking the yield stress σ_Y with equivalent plastic strain $\bar{\varepsilon}$, equivalent plastic strain rate $\dot{\bar{\varepsilon}}$ and temperature θ.

The equations of the problem will be stated in an alternative reference frame $\{X_1, X_2\}$ defined by the fixed angle Ψ between X and X_1 (Fig. 1). Eulerian coordinates with respect to this reference frame are x_1 and x_2. The unknowns of the problem are: velocities (v_1, v_2), strain rates (d_{11}, d_{22}, d_{33}, d_{12}), thickness (h), uniform stresses (σ^u_{11}, σ^u_{22}, σ^u_{12}), through thickness averaged stress (σ^{avg}_{11}), equivalent stress ($\bar{\sigma}$), yield stress (σ_Y), equivalent strain ($\bar{\varepsilon}$), equivalent strain rate ($\dot{\bar{\varepsilon}}$), rate of plastic multiplier ($\dot{\kappa}$), temperature (θ) and the argument of the Bridgman's correction factor (ϕ). The difference between uniform and averaged stresses are defined in Appendix B. From now on, the uniform stresses will be written without the superscript ^{u} for simplicity. The fundamental equations governing the loading process are presented below:

- Rate of deformation tensor

$$d_{11} = \frac{\partial v_1}{\partial x_1} \tag{1}$$

$$d_{22} = \frac{\partial v_2}{\partial x_2} \tag{2}$$

$$d_{12} = \frac{1}{2}\left(\frac{\partial v_1}{\partial x_2} + \frac{\partial v_2}{\partial x_1}\right) \tag{3}$$

- Thickness

$$h = h^0 e^{\varepsilon_3} \tag{4}$$

with $\varepsilon_3 = \varepsilon_z$.

- Yield condition (using uniform stresses, see Appendix B)

$$f = \bar{\sigma} - \sigma_Y \left(\bar{\varepsilon}, \dot{\bar{\varepsilon}}, \theta\right) = 0 \tag{5}$$

- Equivalent stress

$$\bar{\sigma} = \sqrt{\sigma_{11}^2 + \sigma_{22}^2 - \sigma_{11}\sigma_{22} + \frac{3}{2}\left(\sigma_{12}^2 + \sigma_{21}^2\right)} \tag{6}$$

- Equivalent strain rate and equivalent strain

$$\dot{\bar{\varepsilon}} = \sqrt{\frac{2}{3}\mathbf{d} : \mathbf{d}} = \sqrt{\frac{2}{3}\left(d_{11}^2 + d_{22}^2 + d_{33}^2 + 2d_{12}^2\right)} \tag{7}$$

$$\bar{\varepsilon} = \int_0^t \dot{\bar{\varepsilon}}\left(\tau\right) d\tau \tag{8}$$

- Hardening law

$$\sigma_Y \left(\bar{\varepsilon}, \dot{\bar{\varepsilon}}, \theta\right) = \sigma_{y0} \bar{\varepsilon}^n \left(\frac{\dot{\bar{\varepsilon}}}{\dot{\bar{\varepsilon}}_{ref}}\right)^m \left(\frac{\theta}{\theta_{ref}}\right)^\nu \tag{9}$$

where σ_{y0} is a material parameter. Moreover n, m and ν are constants which represent the strain, strain rate and temperature sensitivities of the material. $\dot{\bar{\varepsilon}}_{ref}$ and θ_{ref} are a reference strain rate and a reference temperature respectively.

- Flow rule (using uniform stresses, see Appendix B)

$$d_{11} = \dot{\kappa}\ \frac{2\sigma_{11} - \sigma_{22}}{2\bar{\sigma}} \tag{10}$$

$$d_{22} = \dot{\kappa}\ \frac{2\sigma_{22} - \sigma_{11}}{2\bar{\sigma}} \tag{11}$$

$$d_{12} = \dot{\kappa}\ \frac{3\sigma_{12}}{2\bar{\sigma}} \tag{12}$$

- Incompressibility

$$d_{33} = -d_{11} - d_{22} \tag{13}$$

- Momentum (using averaged stresses, see Appendix B)

$$\frac{\partial\left(h\sigma_{11}^{avg}\right)}{\partial x_1} + \frac{\partial\left(h\sigma_{12}\right)}{\partial x_2} = \rho h \frac{Dv_1}{Dt} \tag{14}$$

$$\frac{\partial\left(h\sigma_{12}\right)}{\partial x_1} + \frac{\partial\left(h\sigma_{22}\right)}{\partial x_2} = \rho h \frac{Dv_2}{Dt} \tag{15}$$

The momentum balance equation in the out of plane direction has been disregarded. For thin plates, it can be shown that the value of the hydrostatic stress linked to the through-thickness acceleration of particles, of order $\rho\dot{\bar{\varepsilon}}\left(h/2\right)^2$, is negligible as compared to the yield stress characteristic of most metal alloys.

Likewise the shear stresses σ_{13} and σ_{23} are negligible according to the results of the finite element model described below, as a result of the small thickness of the plate. Therefore, these shear components are not considered in the momentum balance.

- Energy

$$c\dot{\theta} = k\left(\frac{\partial^2\theta}{\partial x_1^2} + \frac{\partial^2\theta}{\partial x_2^2}\right) + \frac{k}{h}\left(\frac{\partial\theta}{\partial x_1}\frac{\partial h}{\partial x_1} + \frac{\partial\theta}{\partial x_2}\frac{\partial h}{\partial x_2}\right) + \beta\bar{\sigma}\dot{\bar{\varepsilon}} \tag{16}$$

  where c, k and β are heat capacity per unit volume, thermal conductivity and Taylor-Quinney coefficient, respectively.

- Relation between uniform and averaged stresses in direction x_1 (see Appendix B)

$$\sigma_{11}^{avg} = \sigma_{11} B_1(\phi) \tag{17}$$

- Argument of Bridgman's correction factor (see Appendix B)

$$\phi = \frac{a}{2R} = \frac{h}{8}\frac{\partial^2 h}{\partial x_1^2} \tag{18}$$

In previous equations all spatial derivatives are relative to the Eulerian frame, and $\dot{\theta}$, $\dot{\bar{\varepsilon}}$, Dv_1/Dt and Dv_2/Dt are material derivatives.

The equations (1-18) are to be solved under the following initial and boundary conditions:

$$v_x(x,y,0) = \dot{\varepsilon}_x^0 x \ ; \quad v_y(x,y,0) = \dot{\varepsilon}_y^0 y \ ; \quad \sigma_{ij}(x,y,0) = 0$$

$$\bar{\varepsilon}(x,y,0) = 0 \ ; \quad \theta(x,y,0) = \theta^0 \ ; \quad h(x,y,0) = h^0$$

$$v_x\left(\left(1+\dot{\varepsilon}_x^0 t\right) L_x^0/2, y, t\right) = -v_x\left(-\left(1+\dot{\varepsilon}_x^0 t\right) L_x^0/2, y, t\right) = \frac{\dot{\varepsilon}_x^0 L_x^0}{2}$$

$$v_y(x, \left(1+\dot{\varepsilon}_y^0 t\right) L_y^0/2, t) = -v_y(x, -\left(1+\dot{\varepsilon}_y^0 t\right) L_x^0/2, t) = \frac{\dot{\varepsilon}_y^0 L_y^0}{2}$$

$$\left.\frac{\partial\theta}{\partial x_2}\right|_{x=\pm(1+\dot{\varepsilon}_x^0 t)L_x^0/2} = \left.\frac{\partial\theta}{\partial x_2}\right|_{y=\pm\left(1+\dot{\varepsilon}_y^0 t\right)L_y^0/2} = 0$$

The parameters $\dot{\varepsilon}_x^0$ and $\dot{\varepsilon}_y^0$ define the values of the initial strain rates in the sheet.

3. Linear stability analysis

The linear stability analysis presented next is based on the work of Dudzinski and Molinari (1988, 1991) and includes specific features to account for inertia and stress triaxiality effects inside the necking.

The fundamental solution $\mathbb{S}(x_1, x_2, t)$ of the previous problem is obtained by integration of Eqs.(1-18) satisfying the initial and boundary conditions previously listed. Let $\mathbb{S}^1 = \left(v_i^1, d_{ij}^1, h^1, \sigma_{ij}^1, \sigma_{11}^{avg,1}, \bar{\sigma}^1, \bar{\varepsilon}^1, \dot{\bar{\varepsilon}}^1, \dot{\kappa}^1, \theta^1, \phi^1\right)^T$ be the corresponding value at time t^1, when a small perturbation $\delta\mathbb{S}$ given by

$$\delta\mathbb{S}(X_1, t; t^1) = \delta\mathbb{S}^1 e^{i\xi^{\mathscr{L}} X_1} e^{\eta(t-t^1)} \tag{19}$$

is imposed over the fundamental solution, where

$$\delta\mathbb{S}^1 = (\delta v_i, \delta d_{ij}, \delta h, \delta\sigma_{ij}, \delta\sigma_{11}^{avg}, \delta\bar{\sigma}, \delta\bar{\varepsilon}, \delta\dot{\bar{\varepsilon}}, \delta\dot{\kappa}, \delta\theta, \delta\phi)^T \tag{20}$$

is the perturbation amplitude, $\xi^{\mathscr{L}}$ the wavenumber in the Lagrangian configuration and η the growth rate of the perturbation at time t^1. The perturbation is imposed in the Lagrangian coordinate X_1 to guarantee that it follows the material points.

The physical solution is the real part of

$$\mathbb{S} = \mathbb{S}^1 + \delta\mathbb{S} \tag{21}$$

with $|\delta\mathbb{S}| \ll |\mathbb{S}^1|$. By substituting Eq. (21) into Eqs. (1-18) and retaining only first-order terms, linearized equations are obtained. Additionally, five unknowns and equations are removed from the formulation upon linearization, namely:

1. Rate of plastic multiplier: from Eqs. (6), (7) and (10-12) we may derive the equality between equivalent strain rate and rate of plastic multiplier. Thus we may use $\dot{\bar{\varepsilon}}$ instead of $\dot{\kappa}$ in the flow rule and omit Eq. (7).

2. Shell thickness: Linearization of Eq. (4) leads to

$$\delta h = \frac{h^1}{\eta}\delta d_{33} \tag{22}$$

where the following relation has been used

$$\delta\varepsilon_3 = \frac{\delta d_{33}}{\eta} \tag{23}$$

which allows to write δh in terms of δd_{33}.

3. Equivalent strain: Differentiation and linearization of Eq. (8) leads to

$$\delta\dot{\bar{\varepsilon}} = \eta\delta\bar{\varepsilon} \tag{24}$$

and $\delta\bar{\varepsilon}$ may be written in terms of $\delta\dot{\bar{\varepsilon}}$.

4. Averaged stress: σ_{11}^{avg} is written in terms of the uniform stress σ_{11} using Eq. (17).
5. Yield stress: Eq. (5) stated the equivalence between $\bar{\sigma}$ and σ_Y upon deformation, and we may omit the yield stress in the equations.

Finally 13 unknowns are kept, namely (in non-dimensional form)

$$\hat{h} = \frac{h}{h^0}\ ; \qquad \hat{v}_i = \frac{v_i}{h^0\dot{\bar{\varepsilon}}^1}\ ; \qquad \hat{d}_{ij} = \frac{d_{ij}}{\dot{\bar{\varepsilon}}^1}\ ; \qquad \hat{\dot{\bar{\varepsilon}}} = \frac{\dot{\bar{\varepsilon}}}{\dot{\bar{\varepsilon}}^1}$$

$$\hat{\sigma}_{ij} = \frac{\sigma_{ij}}{\sigma_{y0}}\ ; \qquad \hat{\bar{\sigma}} = \frac{\bar{\sigma}}{\sigma_{y0}}\ ; \qquad \hat{\theta} = \frac{\theta}{\theta^0}\ ; \qquad \phi$$

with $i, j = 1, 2$. Likewise, the non-dimensional variables defining the perturbation, together with the perturbation angle $\Psi^{\mathscr{L}}$, are

$$\hat{\eta} = \frac{\eta}{\dot{\bar{\varepsilon}}^1}\ ; \qquad \hat{\xi}^{\mathscr{L}} = \xi^{\mathscr{L}} h^0$$

The choice of $\dot{\bar{\varepsilon}}^1$ as a coefficient for $\hat{\eta}$ permits to compare the growth rate of the perturbation with the deformation rate of the background solution at perturbation time.

The non-dimensional linearized equations are presented afterwards (see Appendix C for details on spatial derivation of a perturbation in a 2D Lagrangian frame).

- Rate of deformation tensor

$$\Lambda^1 \delta\hat{d}_{11} - i\hat{\xi}^{\mathscr{L}} F^1_{22} \delta\hat{v}_1 = 0 \tag{25}$$

$$\Lambda^1 \delta\hat{d}_{22} + i\hat{\xi}^{\mathscr{L}} F^1_{12} \delta\hat{v}_2 = 0 \tag{26}$$

$$\Lambda^1 \delta\hat{d}_{12} + \frac{1}{2} i\hat{\xi}^{\mathscr{L}} F^1_{12} \delta\hat{v}_1 - \frac{1}{2} i\hat{\xi}^{\mathscr{L}} F^1_{22} \delta\hat{v}_2 = 0 \tag{27}$$

  with

$$\Lambda^1 = F^1_{11} F^1_{22} - F^1_{12} F^1_{21} \tag{28}$$

  and F^1_{ij} the components of the deformation gradient at perturbation (see Appendix C).

- Equivalent stress

$$\hat{\bar{\sigma}}^1 \delta\hat{\bar{\sigma}} - \frac{2\hat{\sigma}^1_{11} - \hat{\sigma}^1_{22}}{2} \delta\hat{\sigma}_{11} - \frac{2\hat{\sigma}^1_{22} - \hat{\sigma}^1_{11}}{2} \delta\hat{\sigma}_{22} - 3\hat{\sigma}^1_{12} \delta\hat{\sigma}_{12} = 0 \tag{29}$$

- Hardening law

$$\eta \delta\hat{\bar{\sigma}} - \left(\frac{n}{\bar{\varepsilon}^1} + m\hat{\eta} \right) \hat{\bar{\sigma}}^1 \delta\hat{\bar{\varepsilon}} - \hat{\eta} \frac{\nu \hat{\bar{\sigma}}^1}{\hat{\theta}^1} \delta\hat{\theta} = 0 \tag{30}$$

- Flow rule

$$\hat{d}_{11}^{1}\delta\hat{\bar{\sigma}} + \hat{\bar{\sigma}}^{1}\delta\hat{d}_{11} - \delta\hat{\sigma}_{11} + \frac{1}{2}\delta\hat{\sigma}_{22} - \frac{2\hat{\sigma}_{11}^{1} - \hat{\sigma}_{22}^{1}}{2}\delta\hat{\dot{\bar{\varepsilon}}} = 0 \tag{31}$$

$$\hat{d}_{22}^{1}\delta\hat{\bar{\sigma}} + \hat{\bar{\sigma}}^{1}\delta\hat{d}_{22} - \delta\hat{\sigma}_{22} + \frac{1}{2}\delta\hat{\sigma}_{11} - \frac{2\hat{\sigma}_{22}^{1} - \hat{\sigma}_{11}^{1}}{2}\delta\hat{\dot{\bar{\varepsilon}}} = 0 \tag{32}$$

$$\hat{d}_{12}^{1}\delta\hat{\bar{\sigma}} + \hat{\bar{\sigma}}^{1}\delta\hat{d}_{12} - \frac{3}{2}\delta\hat{\sigma}_{12} - \frac{3\hat{\sigma}_{12}^{1}}{2}\delta\hat{\dot{\bar{\varepsilon}}} = 0 \tag{33}$$

- Incompressibility

$$\delta\hat{d}_{11} + \delta\hat{d}_{22} + \delta\hat{d}_{33} = 0 \tag{34}$$

- Momentum

$$\left(F_{22}^{1}\hat{\sigma}_{11}^{1} - F_{12}^{1}\hat{\sigma}_{12}^{1}\right)\delta\hat{d}_{33} + F_{22}^{1}\hat{\eta}\delta\hat{\sigma}_{11} - F_{12}^{1}\hat{\eta}\delta\hat{\sigma}_{12} + \frac{2}{3}F_{22}^{1}\hat{\sigma}_{11}^{1}\hat{\eta}\delta\phi - \frac{1}{\tilde{I}^{2}}\frac{\Lambda^{1}\hat{\eta}^{2}}{i\hat{\xi}^{\mathscr{L}}}\delta\hat{v}_{1} = 0 \tag{35}$$

$$\left(F_{22}^{1}\hat{\sigma}_{12}^{1} - F_{12}^{1}\hat{\sigma}_{22}^{1}\right)\delta\hat{d}_{33} + F_{22}^{1}\hat{\eta}\delta\hat{\sigma}_{12} - F_{12}^{1}\hat{\eta}\delta\hat{\sigma}_{22} - \frac{1}{\tilde{I}^{2}}\frac{\Lambda^{1}\hat{\eta}^{2}}{i\hat{\xi}^{\mathscr{L}}}\delta\hat{v}_{2} = 0 \tag{36}$$

where

$$\frac{1}{\tilde{I}^{2}} = \frac{\rho\left(h^{0}\dot{\bar{\varepsilon}}^{1}\right)^{2}}{\sigma_{y0}} \tag{37}$$

represents the inertial resistance to motion.

- Energy

$$-\left[\tilde{c}\left(\Lambda^1\right)^2\hat{\eta}+\tilde{k}\left(\left(F^1_{22}\right)^2+\left(F^1_{12}\right)^2\right)(\hat{\xi}^{\mathscr{L}})^2\right]\delta\hat{\theta}+\beta\left(\Lambda^1\right)^2\hat{\bar{\sigma}}^1\delta\hat{\bar{\varepsilon}}+\beta\left(\Lambda^1\right)^2\delta\hat{\bar{\sigma}}=0 \quad (38)$$

with

$$\tilde{k}=\frac{\theta^0 k}{\sigma_{y0}(h^0)^2\dot{\bar{\varepsilon}}^1} \quad (39)$$

$$\tilde{c}=\frac{\theta^0 c}{\sigma_{y0}} \quad (40)$$

- Ratio of neck radius to neck curvature radius

$$8\left(\Lambda^1\right)^2\hat{\eta}\delta\phi+\left(\hat{h}^1\hat{\xi}^{\mathscr{L}}F^1_{22}\right)^2\delta\hat{d}_{33}=0 \quad (41)$$

A non-trivial solution for $\delta\hat{\mathbb{S}}^1$ is obtained only if the determinant of the system of linear algebraic equations (25-27), (29-36), (38) and (41) is equal to zero. This condition is found to be a fifth-degree polynomial in $\hat{\eta}(\hat{\xi}^{\mathscr{L}})$ which gives, for a certain value of the time at perturbation t^1, the value of $\hat{\eta}$ as a function of the dimensionless wavenumber in the material description $\hat{\xi}^{\mathscr{L}}$. The requisite for unstable growth of $\delta\mathbb{S}$ is given by the condition $Re\,(\bar{\eta})>0$. The quoted polynomial has five roots in $\hat{\eta}$ among which the one that is real and positive $\hat{\eta}^+$ (which also shows the maximum real part) represents the unstable growth. Note that, according to Rodríguez-Martínez et al. (2013c, 2015b) the perturbation growth η^+ is assumed to represent the onset of *diffuse necking*, the very first stages at which the plastic flow deviates from the background deformation. Moreover, imposing the condition for maximum perturbation growth $\partial\hat{\eta}^+/\partial\hat{\xi}^{\mathscr{L}}=0$, the critical wavenumber $\hat{\xi}^{\mathscr{L}}_c$ and the critical perturbation growth $\hat{\eta}^+_c$ are determined.

4. Finite element modelling of the dynamic biaxial loading of a thermoviscoplastic sheet

This section describes the features of the finite element model developed to simulate the rapid stretching of a ductile sheet. The numerical analyses are carried out using the finite element program ABAQUS/Explicit (Simulia, 2013a). The reference configuration of the sheet is given by the domain $-L_x^0/2 \leq X \leq L_x^0/2$, $-L_y^0/2 \leq Y \leq L_y^0/2$ and $-h^0/2 \leq Z \leq h^0/2$, with $L_x^0 = L_y^0 = 50\ mm$ and $h^0 = 2\ mm$. Due to the symmetry of the problem with respect to the plane $Z = 0$, only the $Z \geq 0$ half of the specimen has been analyzed. The sheet has been meshed using a total of 63075 eight-node reduced integration elements (C3D8R in ABAQUS notation), 145 in X and Y directions, and 3 in Z direction. Following the considerations reported by Zukas and Scheffer (2000) the element aspect ratio is $\sim 1:1:1$. To prevent hourglass deformation modes, the viscous method available in ABAQUS/Explicit has been used, with a scale factor for all hourglass stiffnesses equal to one.

A mesh sensitivity analysis was performed, considering the initial loading rate $\dot{\bar{\varepsilon}}^0 = 5000\ s^{-1}$ and isothermal conditions ($\beta = 0$). This loading and material configuration leads to the greatest values of necking strain examined in this paper (greatest elements deformation), and therefore to the most adverse working conditions for the mesh. We have checked that obtaining mesh independent results (in terms of stress, strain and necking inception) for this loading and material configuration implies obtaining mesh independent results for any other configuration investigated in this paper.

The imposed loading conditions are:

$$\begin{aligned} V_x(L_x^0/2, Y, t) &= -V_x(-L_x^0/2, Y, t) = \dot{\varepsilon}_x^0 L_x^0/2 \\ V_y(X, L_y^0/2, t) &= -V_y(X, -L_y^0/2, t) = \dot{\varepsilon}_y^0 L_y^0/2 \end{aligned} \tag{42}$$

In order to avoid the spurious propagation of waves along the plate, caused by the application of these boundary conditions in a solid at rest, specific initial conditions consistent with the boundary conditions are imposed (see Zaera et al. (2014) for detailed explanation of these initial conditions)

$$V_x(X,Y,0) = \dot{\varepsilon}_x^0 X$$
$$V_y(X,Y,0) = \dot{\varepsilon}_y^0 Y$$
$$V_z(X,Y,0) = -\left(\dot{\varepsilon}_x^0 + \dot{\varepsilon}_y^0\right) Z \tag{43}$$

Neither geometrical nor material imperfections were introduced into the model, being the numerical round-off sufficient to perturb the field variables (Rusinek and Zaera, 2007; Vadillo et al., 2012; Rodríguez-Martínez et al., 2013b). Regarding initial thermal conditions, θ^0 has been taken equal to 293 K in all cases. The whole model was defined with a script to allow the rapid definition of initial and boundary conditions in consonance with the particular loading case considered.

Table 3 shows the parameters of the baseline material, representative of an HRS steel (Clifton et al., 1984), that are used in both stability and FE analyses, unless otherwise stated. The set of equations describing the thermoviscoplastic behaviour of the material are implemented in the finite element code, considering a large deformation frame, through a user subroutine following the fully implicit integration scheme developed by Zaera and Fernández-Sáez (2006).

5. Salient features of the stability analysis

In this section the main features of the stability analysis are presented and discussed. For simplicity, this is conducted under isothermal conditions ($\beta = 0$), thus avoiding thermal softening and heat flow. The loading and perturbation conditions are selected through the values of the initial equivalent strain rate $\dot{\bar{\varepsilon}}^0$, the strain in direction X at perturbation (ε_x^1), and the ratio of strains in directions Y and X at perturbation ($\chi_\varepsilon^1 = \varepsilon_y^1/\varepsilon_x^1$). The first one permits to select the rate at which the sheet is loaded, and the other two the state of deformation at which the stability of the perturbation is analysed. Using Eq. (7) in directions $\{X, Y\}$ at $t = 0$, and Eqs. (A.10) and (A.16) at $t = t^1$, we may derive $\dot{\varepsilon}_x^0$ and $\dot{\varepsilon}_y^0$ to set the loading conditions, and t^1 to set the perturbation time. The kinematic variables of the homogeneous solution are then explicitly obtained with the equations given in Appendix A, while the homogeneous stress and temperature fields are obtained

Symbol	Property and units	Value
σ_{y0}	Material parameter (MPa), Eq. (9)	710
n	Strain hardening exponent, Eq. (9)	0.12
m	Strain rate sensitivity exponent, Eq. (9)	0.0133
ν	Temperature sensitivity exponent, Eq. (9)	-0.51
θ_{ref}	Reference temperature (K), Eq. (9)	293
$\dot{\bar{\varepsilon}}_{ref}$	Reference strain rate (s^{-1}), Eq. (9)	10^{-3}
β	Taylor–Quinney coefficient, Eq. (16)	0.9
k	Thermal conductivity ($WK^{-1}m^{-1}$), Eq. (16)	16
c	Specific heat ($MJK^{-1}m^{-3)}$, Eq. (16)	3.61
ρ	Material density ($kg\ m^{-3}$), Eq. (16)	7850
E	Young modulus (GPa)	200
μ	Poisson ratio	0.33

Table 3: *Material properties representative of the HRS steel (Clifton et al., 1984).*

by integration of governing equations. The ratio of strain rates at $t = 0$ is given by $\chi_{\dot{\varepsilon}}^0 = \dot{\varepsilon}_y^0/\dot{\varepsilon}_x^0$.

5.1. Critical perturbation growth

Figure 2 shows the dimensionless perturbation growth $\hat{\eta}^+$ versus the dimensionless wavenumber $\hat{\xi}^{\mathscr{L}}$. The initial equivalent strain rate has been set to $\dot{\bar{\varepsilon}}^0 = 1000\ s^{-1}$, and the perturbation is imposed at $\varepsilon_x^1 = 0.3$ and $\chi_\varepsilon^1 = 0$ (plane strain in direction Y). An orientation described in Lagrangian coordinates $\Psi^{\mathscr{L}} = 0°$ is considered for the perturbation. To be noted that in this particular case Lagrangian and Eulerian descriptions coincide $\Psi^{\mathscr{L}} = \Psi^{\mathscr{E}} = 0°$. In a more general scenario, they are related by Eq. (A.28). Results in which inertia effects and Bridgman correction are alternatively switched on and off are depicted in Fig. 2. We show that inertia slows down the growth of long wavelength perturbations and stress triaxiality slows down the growth of short wavelength perturbations, promoting an intermediate wavelength which determines the critical perturbation growth $\hat{\eta}_c^+$ and critical wavenumber $\hat{\xi}_c^{\mathscr{L}}$. This behaviour, already highlighted elsewhere (Fressengeas and Molinari, 1994; Molinari, 1997; Mercier and Molinari, 2003, 2004; Zhou et al., 2006) for different loading paths, is now confirmed for biaxial loading. Thus, from this point on, we focus our attention on the critical perturbation growth $\hat{\eta}_c^+$ (most unstable material condition for given perturbation orientation Ψ) for the case which considers both inertia and stress multiaxiality effects.

Figure 3 shows the critical perturbation growth $\hat{\eta}_c^+$ versus the direction of perturbation in the Lagrangian configuration $\Psi^{\mathscr{L}}$ for different values of χ_ε^1. The perturbation is imposed at $\varepsilon_x^1 = 0.3$. We show that $\hat{\eta}_c^+$ varies with the direction of perturbation $\Psi^{\mathscr{L}}$. Furthermore, three different scenarios are identified as a function of the value of χ_ε^1.

- $\chi_\varepsilon^1 < 0$. A pair of excursions in the curves $\hat{\eta}_c^+ - \Psi^{\mathscr{L}}$, equidistant from the direction $\Psi^{\mathscr{L}} = 0°$, are observed. The orientation which determines these excursions will be named as the critical direction of perturbation $\Psi_c^{\mathscr{L}}$. As χ_ε^1 approaches zero, $\Psi_c^{\mathscr{L}}$ comes closer to zero. These excursions become sharper and narrower as χ_ε^1 decreases, boosting the dominant character that the critical direction of perturbation shows over the rest of possible orientations of perturbation. Moreover, the value of $\hat{\eta}_c^+$

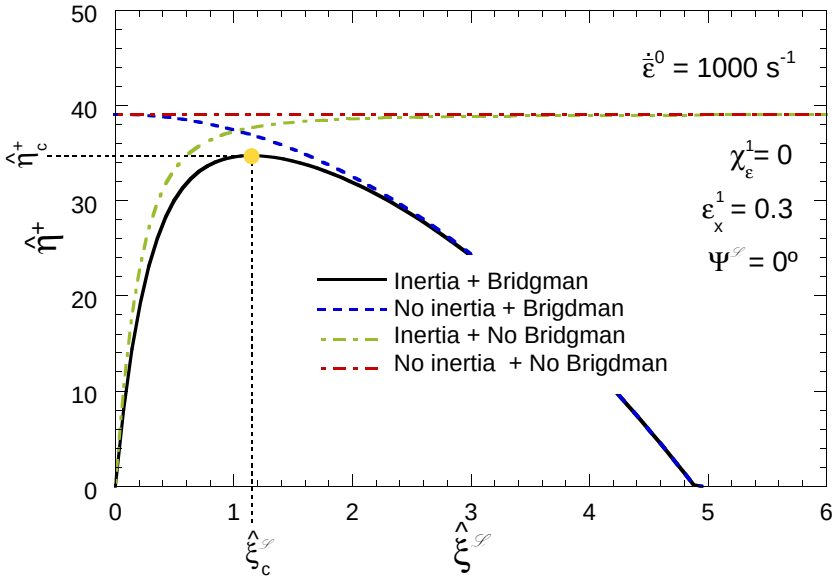

Figure 2: Dimensionless perturbation growth $\hat{\eta}^+$ versus dimensionless wavenumber $\hat{\xi}^{\mathscr{L}}$. Plane strain $\chi_\varepsilon^1 = 0$ and isothermal conditions. Initial equivalent loading rate $\dot{\bar{\varepsilon}}^0 = 1000\ s^{-1}$. Perturbation at $\Psi^{\mathscr{L}} = 0°$.

corresponding to the peaks increases as χ_ε^1 increases.

- $\chi_\varepsilon^1 = 0$. This loading condition corresponds to plane strain. The two excursions obtained for $\chi_\varepsilon^1 < 0$ are now merged into one which is located at $\Psi^{\mathscr{L}} = 0°$. In comparison with the $\chi_\varepsilon^1 < 0$ cases, now: (i) the excursion in the $\hat{\eta}_c^+ - \Psi^{\mathscr{L}}$ curve is wider and blunter, slowing down the dominant character that the critical direction of perturbation shows over the rest of perturbation orientations; (ii) the value of $\hat{\eta}_c^+$ obtained for $\Psi_c^{\mathscr{L}}$ is larger.

- $\chi_\varepsilon^1 > 0$. One excursion in the curve $\hat{\eta}_c^+ - \Psi^{\mathscr{L}}$, located at $\Psi^{\mathscr{L}} = 0°$, is obtained. In comparison with the $\chi_\varepsilon^1 = 0$ case, now: (i) the excursion in the $\hat{\eta}_c^+ - \Psi^{\mathscr{L}}$ curve is wider and blunter, slowing down the dominant character that the critical direction of perturbation shows over the rest of perturbation directions; (ii) the value of $\hat{\eta}_c^+$ obtained for $\Psi_c^{\mathscr{L}}$ is smaller.

Thus, from this point on, we focus our attention on the critical perturbation growth $\hat{\eta}_c^+$ corresponding to the critical orientation $\Psi_c^{\mathscr{L}}$ (most unstable material condition for given ratio of strains χ_ε). The following conclusions can be derived from previous analysis:

1. The maximum value of the critical perturbation growth corresponds to plane strain ($\chi^1_\varepsilon = 0$). Therefore, this loading path determines the most unstable material condition. In other words, the minimum necking strain shall correspond to plane strain.
2. The critical perturbation growth gradually decreases as the loading path gets away from plane strain, which stabilizes material behaviour. In other words, the necking strain shall increase as the loading path moves away from $\chi^1_\varepsilon = 0$.
3. For strain paths with $\chi^1_\varepsilon \geq 0$ only one family of parallel necks shall develop, whereas two families of parallel necks shall emerge for strain paths with $\chi^1_\varepsilon < 0$.

It is worth to point out that the critical direction of perturbation $\Psi^{\mathscr{L}}_c$, obtained with the stability analysis, coincides with the direction of zero stretch rate if $\chi^1_\varepsilon \leq 0$. This direction was identified by Stören and Rice (1975), using a bifurcation analysis, as that corresponding to the development of the neck. If $d^1_{yy}/d^1_{xx} < 0$ we find two directions of zero stretch rate. In the deformed configuration, the angles of these directions with respect to the X axis (with $d^1_{xx} > d^1_{yy}$) are given by

$$\varphi^{\mathscr{E}}_{\dot{\varepsilon}=0} = \frac{\pi}{2} \pm \frac{1}{2}\arccos\left(\frac{d^1_{xx} + d^1_{yy}}{d^1_{xx} - d^1_{yy}}\right) \tag{44}$$

A pull back of these directions to the reference configuration, using the inverse of expression (A.28), permits to compare their values with the critical direction of perturbation, finding perfect agreement, as can be observed in Fig. 3.

In order to provide further insights into previous observations, we adopt the following procedure developed by Dudzinski and Molinari (1991). Let us consider a given ratio of strains at perturbation χ^1_ε and a given positive number $\boldsymbol{e}$. The values (if they exist) $\varepsilon_x(\boldsymbol{e}, \chi^1_\varepsilon, \Psi^{\mathscr{L}}_c)$ and $\varepsilon_y(\boldsymbol{e}, \chi^1_\varepsilon, \Psi^{\mathscr{L}}_c)$ of strains in principal directions X and Y are considered, for which $\hat{\eta}^+_c$ satisfies the relation $\hat{\eta}^+_c = \boldsymbol{e}$. When this condition is realized, the critical mode associated to the Lagrangian critical orientation $\Psi^{\mathscr{L}}_c$ and the ratio of strains at perturbation χ^1_ε is said to present an effective instability of intensity $\boldsymbol{e}$, or an effective $\boldsymbol{e}$–instability. Then, the parameter $\boldsymbol{e}$ introduced is a measure of the rate of growth of the most critical perturbation mode for a given ratio of strains at perturbation χ^1_ε. In other words, among all the unstable modes for given χ^1_ε, we are selecting those attaining a growth

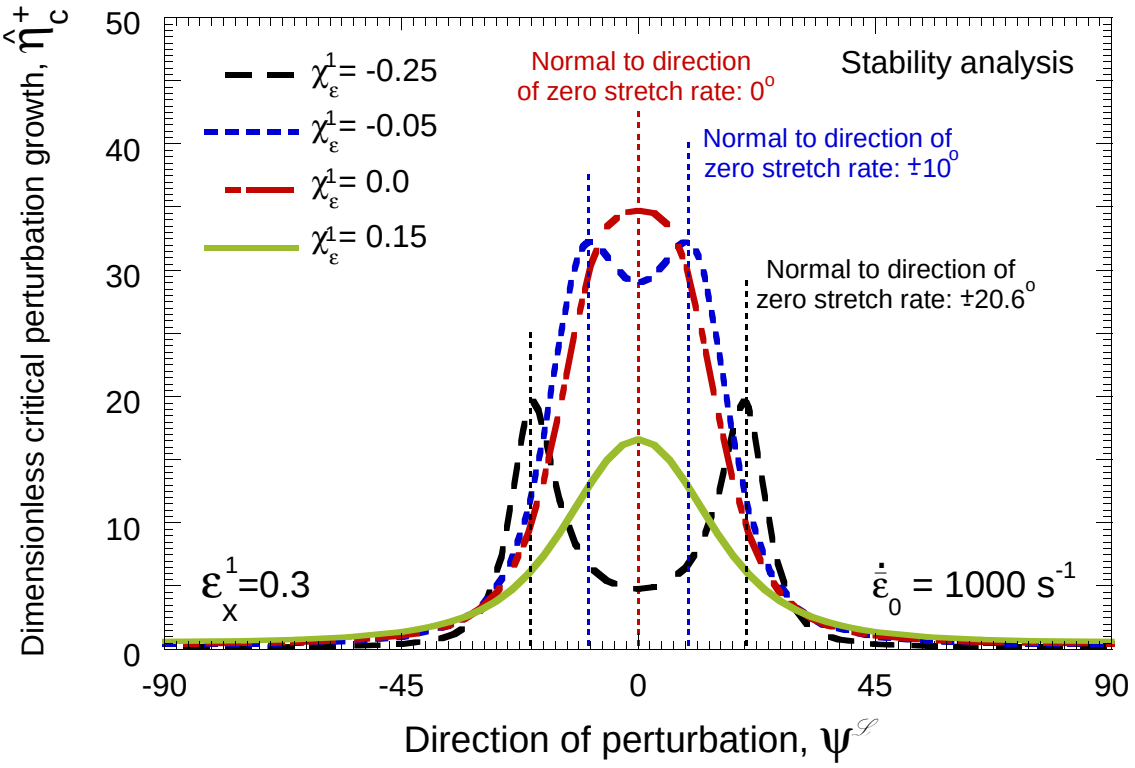

Figure 3: Critical perturbation growth $\hat{\eta}_c^+$ versus direction of perturbation $\Psi^{\mathscr{L}}$ for different values of the ratio of strains at perturbation: $\chi_\varepsilon^1 = -0.25$, $\chi_\varepsilon^1 = -0.05$, $\chi_\varepsilon^1 = 0.0$ and $\chi_\varepsilon^1 = 0.15$. For the cases in which $\chi_\varepsilon^1 \leq 0$ the corresponding directions of zero strain rate, Eq. (A.5), are shown. Initial equivalent loading rate $\dot{\bar{\varepsilon}}^0 = 1000\ s^{-1}$ and isothermal conditions.

rate equal to $\boldsymbol{e}$. The corresponding strain ε_x^1 can be roughly viewed as the strain for which the instability develops a growth rate equal to $\boldsymbol{e}$ (and provides a qualitative idea of the material necking strain for given χ_ε^1 as further discussed in this paper).

Thus, following this scheme, Fig. 4 shows the perturbation strain in principal direction X versus the perturbation strain in principal direction Y for different values of the effective $\boldsymbol{e}$–instability. It has to be noted that this type of graph (ε_x^1 versus ε_y^1) follows the scheme used to represent forming limit diagrams (FLDs), in which the major and minor in-plane principal strains are confronted. Several comments arise from these calculations which, for the sake of clarity, are organized as follows:

1. Influence of the minor in-plane principal strain ε_y^1: (*i*) The minimum value of ε_x^1 is obtained for plane strain $\varepsilon_y^1 = 0$, i.e. plane strain conditions lead to the most unstable material condition which shall correspond with the minimum necking strain. (*ii*) Moving along ε_y^1 axis from plane strain to positive values of ε_y^1 means an increase in ε_x^1, i.e. positive values of ε_y^1 lead to material stabilization which shall correspond with an increase in necking strain. (*iii*) To move along ε_y^1 axis from plane strain to negative values means an increase in ε_x^1, i.e. negative values of ε_y^1 lead to material stabilization which shall lead to increasing necking strain.

   These trends agree with those observations anticipated in previous paragraphs. Additionally, it has to be strengthened that these trends build a FLD-type scheme that finds good *qualitative* agreement with experimental results reported in the literature for most metals and alloys.

2. Influence of the effective $\boldsymbol{e}$–instability: (*i*) Increasing the effective $\boldsymbol{e}$–instability moves upwards the $\varepsilon_x^1 - \varepsilon_y^1$ curve, i.e increasing strain boosts material destabilization which agrees with the observations reported in Rodríguez-Martínez et al. (2015b) and Zaera et al. (2014) for uniaxial tension conditions and by Mercier and Molinari (2003) for plain strain. (*ii*) The value of $\boldsymbol{e}$ does not change the fundamental aspects of the interplay between ε_y^1 and ε_x^1, i.e. the analysis reported in previous paragraph is independent of the value of $\boldsymbol{e}$.

   On the one hand, using the effective $\boldsymbol{e}$–instability concept allows to obtain results from the stability analysis that simulate the scheme of FLDs (Dudzinski and Moli-

nari, 1991). On the other hand, this *user-dependent* parameter does not modify qualitatively the results (general trends) derived from the model.

As an additional remark, Fig. 4 shows two strain paths, one for a positive (P_1) and one for a negative (P_2) ratio of strains χ^1_ε. As stated in Appendix A, the kinematics considered for the homogeneous state of deformation leads to non-proportional straining in order to verify uniformity in the stress field. However, the paths are practically straight thus representing adequately a proportional loading $\varepsilon_y/\varepsilon_x \approx constant$ ($\chi_\varepsilon \approx \chi_{\dot\varepsilon}$).

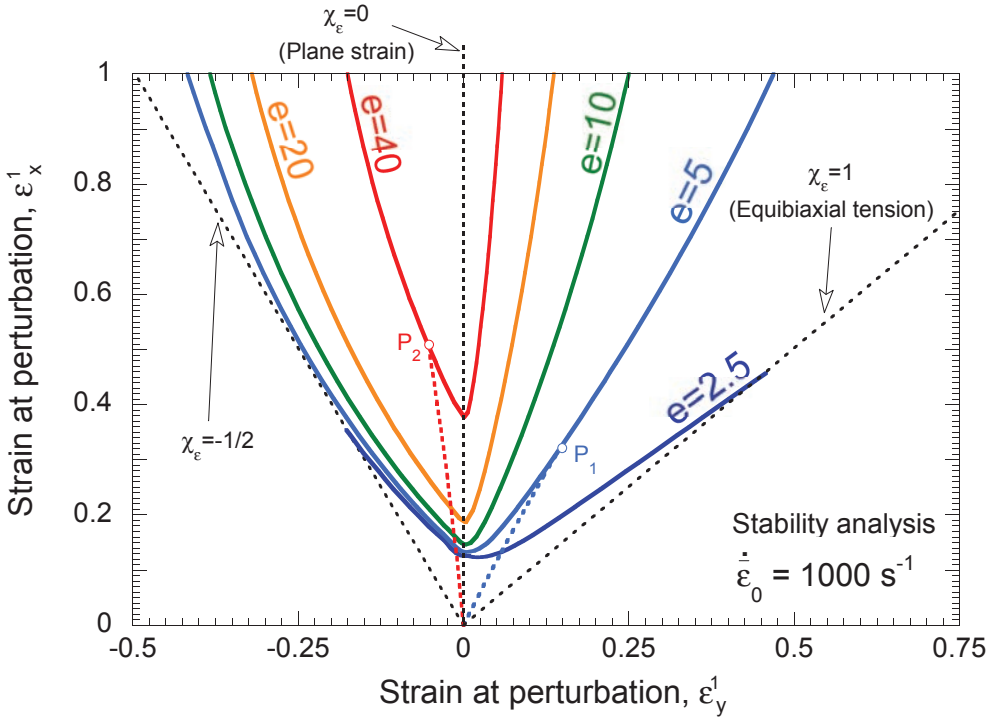

Figure 4: ε^1_x (perturbation strain in principal direction X) versus ε^1_y (perturbation strain in principal direction Y) for different values of the effective $\boldsymbol{e}$–instability: $\boldsymbol{e} = 2.5$, $\boldsymbol{e} = 5$, $\boldsymbol{e} = 10$, $\boldsymbol{e} = 20$ and $\boldsymbol{e} = 40$. Strain paths for two different ratios of strain $\chi^1_\varepsilon > 0$ (P_1) and $\chi^1_\varepsilon < 0$ (P_2). Initial equivalent loading rate $\dot{\bar{\varepsilon}}^0 = 1000\ s^{-1}$ and isothermal conditions.

5.2. Critical direction of perturbation and critical wavenumber

Following the same scheme used to present the values of the effective $\boldsymbol{e}$-instability, Fig. 5 shows the critical direction of perturbation $\Psi_c^{\mathscr{L}}$ in the material description, corresponding to different strains $(\varepsilon^1_y, \varepsilon^1_x)$, calculated with the linear stability analysis. Two different situations are identified as a function of the sign of the value assigned to χ^1_ε:

- $\chi_\varepsilon^1 > 0$. Critical direction of perturbation is defined by $\Psi_c^{\mathscr{L}} = 0$, which means that necking bands are oriented following direction Y.

- $\chi_\varepsilon^1 < 0$. Critical direction of perturbation has a value different than zero. Keeping in mind Fig. 3, necking bands are then oriented along directions forming an angle $\pm\Psi_c^{\mathscr{L}}$ with respect to axis Y. This angle increases with the absolute value of the ratio of strains χ_ε^1.

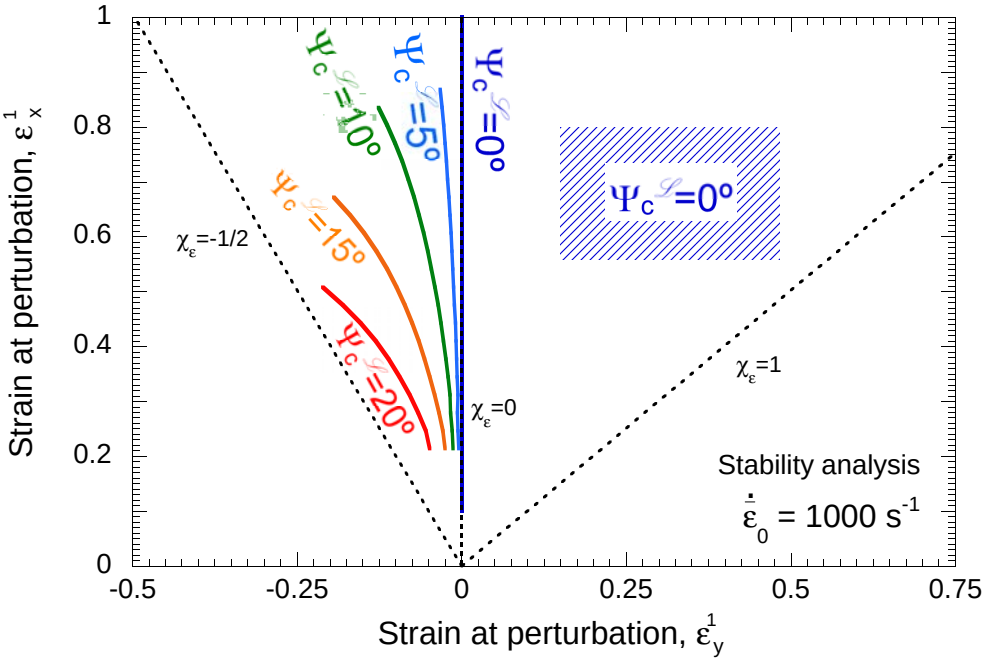

Figure 5: ε_x^1 (perturbation strain in principal direction X) versus ε_y^1 (perturbation strain in principal direction Y) for different values of the critical direction of perturbation: $\Psi_c^{\mathscr{L}} = 0°$, $\Psi_c^{\mathscr{L}} = 5°$, $\Psi_c^{\mathscr{L}} = 10°$, $\Psi_c^{\mathscr{L}} = 15°$ and $\Psi_c^{\mathscr{L}} = 20°$. Initial equivalent loading rate $\dot{\bar{\varepsilon}}^0 = 1000\ s^{-1}$ and isothermal conditions.

Fig. 6 shows the perturbation strain in principal direction X (ε_x^1) versus the perturbation strain in principal direction Y (ε_y^1) for different iso-wavenumber $\hat{\xi}_c^{\mathscr{L}}$ curves. Considering both inertial and triaxial effects allows to derive a critical wavenumber (Fig. 2) that could not be determined otherwise by the linear stability analysis. The iso-wavenumber $\hat{\xi}_c^{\mathscr{L}}$ curves show a minimum for $\varepsilon_y^1 = 0$ and increase as one moves away from plane strain. As we further elaborate in forthcoming sections of this paper, the critical wavenumber allows for calculation of the critical distance between necks. This is one of the salient and

distinctive features of the approach herein presented.

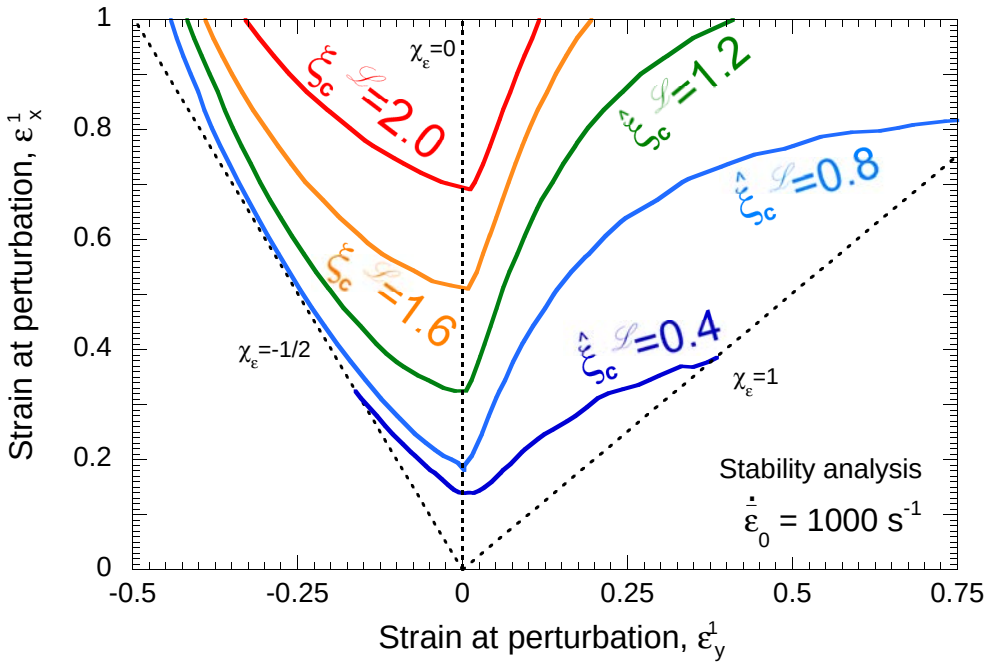

Figure 6: ε_x^1 (perturbation strain in principal direction X) versus ε_y^1 (perturbation strain in principal direction Y) for different iso-wavenumber curves: $\hat{\xi}_c^{\mathscr{L}} = 0.4$, $\hat{\xi}_c^{\mathscr{L}} = 0.8$, $\hat{\xi}_c^{\mathscr{L}} = 1.2$, $\hat{\xi}_c^{\mathscr{L}} = 1.6$ and $\hat{\xi}_c^{\mathscr{L}} = 2.0$. Initial equivalent loading rate $\dot{\bar{\varepsilon}}^0 = 1000\ s^{-1}$ and isothermal conditions.

6. Analysis and results

In this section of the paper we show the key outcomes obtained from the finite elements and the stability analysis. Our interest is focused on the onset and development of strain localization bands (necking bands), paying specific attention to: (1) the influence of loading path in neck spacing which is investigated in section 6.1, (2) the effect of loading rate which is addressed in section 6.2, and (3) the effect of thermal coupling which is addressed in section 6.3.

As in section 5, we use the reference material parameters listed in Table 3. In Fig. 7 we show results from the finite element calculations and the linear stability analysis (for isothermal conditions $\beta = 0$ and $\dot{\bar{\varepsilon}}^0 = 1000\ s^{-1}$). This figure is considered essential since it illustrates the approach followed in sections 6.1, 6.2 and 6.3.

- Finite element calculations: we illustrate the strain in principal direction X (ε_x^{neck})

versus the strain in principal direction Y (ε_y^{neck}), both measured at diffuse necking. The numerical computations were conducted within the range $|\varepsilon_y^{neck}| \lesssim 0.15$. The term diffuse necking strain (from this point designated indistinctly as necking strain) describes the stage of the loading process at which the local plastic flow deviates from the background value. The diffuse necking is a *measure* of material instability, alternative to the localized necking criterion which is commonly used in computational analyses (Triantafyllidis and Waldenmyer, 2004; Zaera et al., 2014). In the present context, determination of the diffuse necking presents a clear advantage: the diffuse necking strain can be correlated with the perturbation growth in the stability analysis, as mentioned in section 3. Further discussion on the suitability of the diffuse necking criterion to evaluate material instability is developed in Appendix D, where we compare results obtained from both diffuse and localized necking criteria.

The loading time corresponding to the diffuse necking is determined in the simulations as the loading stage for which the first localization pattern appears, i.e. the first time we observe excursions of strain coming out from the fundamental solution. The time corresponding to diffuse necking is inserted into Eqs. (A.10) and (A.16) to obtain (ε_x^{neck}) and (ε_y^{neck}) respectively. Each solid dot in Fig. 7 corresponds to a numerical computation, while the solid line is the fitting curve. There is some scatter in the results that can be explained by the inherent variability of the round-off errors responsible for the numerical perturbations which trigger flow localization. Nevertheless, we claim that the number of simulations that has been carried out is sufficiently large to show reliable/consistent trends in the ε_x^{neck} - ε_y^{neck} graph.

The computations confirm the observations derived from the stability analysis in section 5. On the one hand the numerical calculations indicate that the minimum necking strain is found for plane strain $\varepsilon_y^{neck} = 0$; the loading path for which the stability analysis predicted the most unstable material condition. On the other hand the numerical calculations show that moving along the ε_y^{neck} axis from plane strain to positive/negative values of ε_y^{neck} means a considerable increase in ε_x^{neck}. This observation fully agrees with the stability analysis which predicted that the material becomes stabilized as the absolute value of ε_y^{neck} increases.

- Stability analysis: we illustrate the perturbation strain in principal direction X (ε_x^1) versus the perturbation strain in principal direction Y (ε_y^1) for the effective e-instability $\boldsymbol{e} = 40$ and different values of the Lagrangian critical wavenumber $\hat{\xi}_c^{\mathscr{L}}$. The e-instability curve displays a concave-up shape, similar at some extent to the $\varepsilon_x^{neck} - \varepsilon_y^{neck}$ curve obtained from the numerical computations. The specific curve $\boldsymbol{e} = 40$ is taken since it (roughly) provides the closest approximation (at least near plane strain) to the finite element results. Similarly, we consider the iso-wavenumber curves $\hat{\xi}_c^{\mathscr{L}}$ which lie within the finite element results.

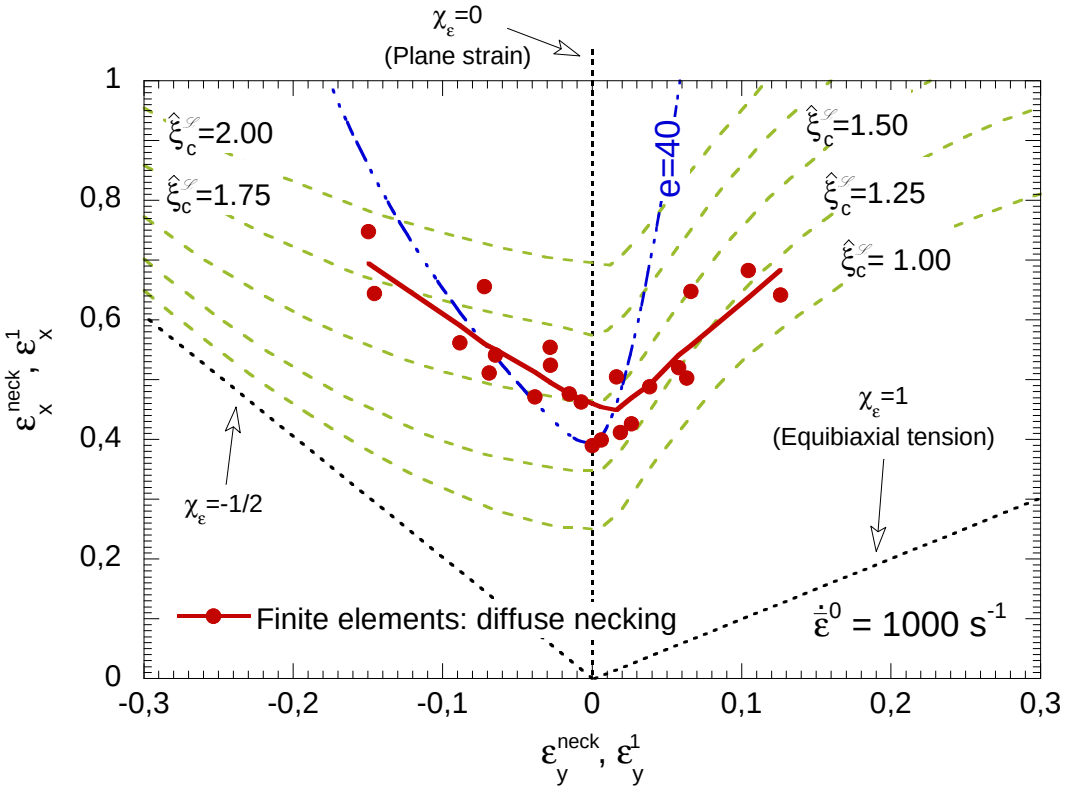

Figure 7: Finite elements: ε_x^{neck} (diffuse necking strain in principal direction X) versus ε_y^{neck} (diffuse necking strain in principal direction Y). Stability analysis: ε_x^1 (perturbation strain in principal direction X) versus ε_y^1 (perturbation strain in principal direction Y) for the effective e-instability $\boldsymbol{e} = 40$ and different values of the critical wavenumber in the *material configuration*: $\hat{\xi}_c^{\mathscr{L}} = 1.00$, $\hat{\xi}_c^{\mathscr{L}} = 1.25$, $\hat{\xi}_c^{\mathscr{L}} = 1.50$, $\hat{\xi}_c^{\mathscr{L}} = 1.75$ and $\hat{\xi}_c^{\mathscr{L}} = 2.00$. Initial equivalent loading rate $\dot{\bar{\varepsilon}}^0 = 1000\ s^{-1}$ and isothermal conditions.

6.1. The effect of loading path on neck spacing

Based on the numerical computations and the stability analysis we follow three different methods to determine the spacing between necking bands.

1. Method 1 (finite elements): we measure the distance between bands $L^{\mathscr{L}}$ directly from the finite element computations. In Fig. 8 we depict contours of equivalent plastic strain $\bar{\varepsilon}$ which show patterns of necking bands in the Lagrangian configuration for different ratios of strain $\chi^0_{\dot{\varepsilon}} = -0.125$ and $\chi^0_{\dot{\varepsilon}} = 0.05$. The dynamic character of the problem makes possible the appearance of multiple localization bands. For each simulation we measure the average distance between necking bands in the Lagrangian configuration $\bar{L}^{\mathscr{L}}$ as a function of the ratio of strains at diffuse necking $\chi^{neck}_{\dot{\varepsilon}}$. The average band spacing is taken in the material description in order to facilitate the comparison with the stability analysis results. In any case investigated, the localization bands are aligned with the critical directions of perturbation (in agreement with the predictions of the stability analysis), and therefore coincident with the directions of zero stretch rate when $\chi^0_{\dot{\varepsilon}} < 0$, (Fig. 5). For $\chi^0_{\dot{\varepsilon}} < 0$ we obtain two families of bands, symmetric to each other with respect to the Y direction, $\left|\Psi^{\mathscr{L}}_c\right| > 0$. This necking pattern finds good qualitative correlation with the experimental evidences reported by Vaz-Romero et al. (2015) who carried out dynamic tensile experiments (i.e. $\chi^0_{\dot{\varepsilon}} < 0$) using steels sheets. For $\chi^0_{\dot{\varepsilon}} \geqslant 0$ we obtain multiple necking bands aligned with the Y direction, $\Psi^{\mathscr{L}}_c = 0$. This necking pattern agrees with the experimental evidences reported by Mercier et al. (2010) who carried out high-rate expansion experiments in hemispherical metallic shells. The authors reported the emergence of multiple necking bands, parallel to each other, within the small layer of the shell which is subjected to plane strain conditions ($\chi^0_{\dot{\varepsilon}} = 0$).

   For $\chi^0_{\dot{\varepsilon}} < 0$ the intersection of necking bands is always observed at the boundaries of the plate. The boundary conditions affect the arrangement and collective behaviour of the localization bands in such manner that each pair of bands meets at the edges of the plate. This result derived from the finite element model is consistent with the experimental finding of Vaz-Romero et al. (2015) who reported the emergence of two families of necking bands following the two directions of zero stretch rate which

intersect at the sample boundaries. It should be noted that the influence of this *spurious* effect of the sample dimensions on the neck spacing gets reduced as the number of localization bands increases. At the limit case of an infinitely large plate (infinite number of bands) the dimensions of the sheet would not play any role in the spacing (as in the stability analysis). Obviously, this ideal case neither can be defined in the finite element computations nor in the experiments, and there will always be some effect of the plate dimensions on the neck spacing. Nevertheless, we have performed calculations using different plate sizes and systematically checked that the plate dimensions used in the simulations reported in this paper provide results largely independent on the plate size.

2. Method 2 (finite elements + stability analysis): we combine the results obtained from the finite elements and the stability analysis to predict the average distance between necking bands. In Fig. 7 each finite element result (each solid dot) corresponds to a value of $\hat{\xi}_c^{\mathscr{L}}$ obtained from the stability analysis. The Lagrangian critical wavenumber is then used to calculate the average Lagrangian band spacing as $\bar{L}^{\mathscr{L}} = \frac{2\pi h^0}{\hat{\xi}_c^{\mathscr{L}}}$.
3. Method 3 (stability analysis): we rely, exclusively, on the stability analysis to predict the distance between bands. Following Dudzinski and Molinari (1991) we evaluate the suitability of the effective e-instability criterion to determine the average band spacing. In Fig. 7, we determine the intersections of $\boldsymbol{e} = 40$ with the critical iso-wavenumer curves. For each intersection point we obtain the ratio of strains at perturbation as a function of $\hat{\xi}_c^{\mathscr{L}}$. The Lagrangian critical wavenumber allows calculation of $\bar{L}^{\mathscr{L}}$ as in method 2.

Method 1 provides the results that will be used as a reference to check the suitability of methods 2 and 3 to predict the average necking band spacing.

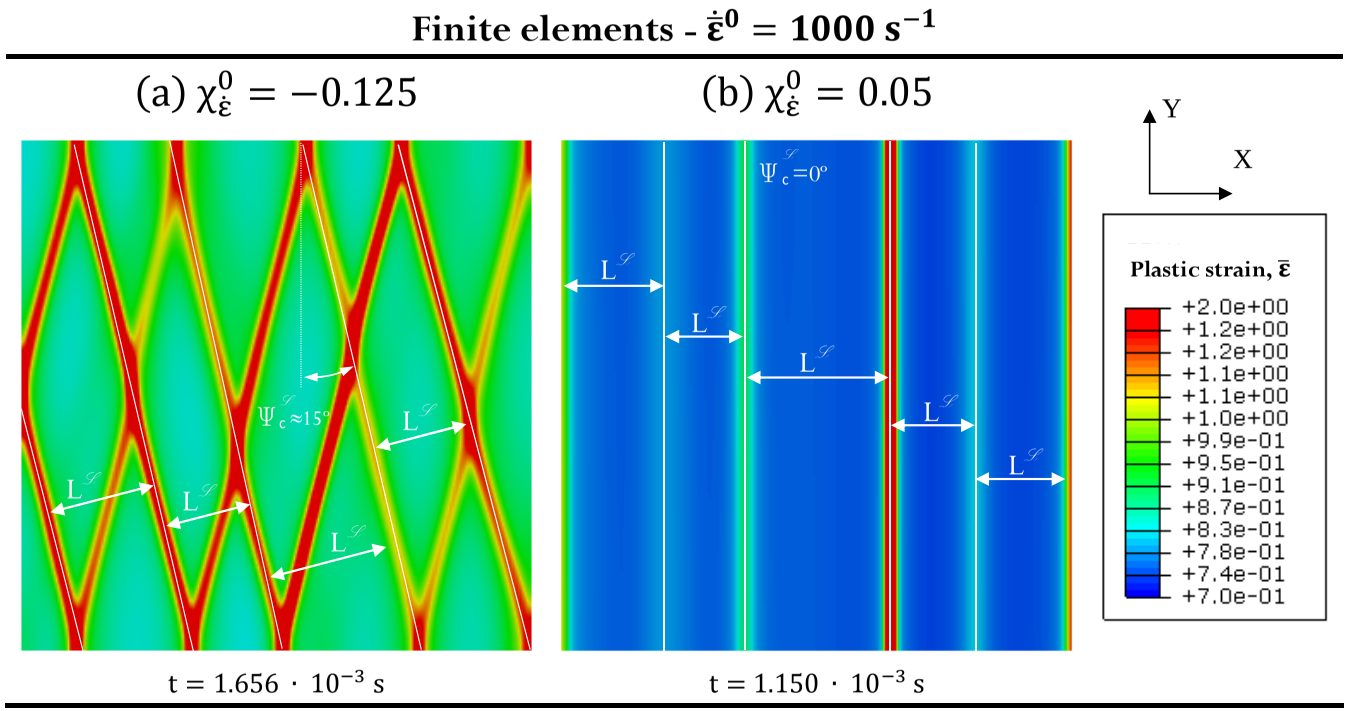

Figure 8: Finite element results. Contours of equivalent plastic strain $\bar{\varepsilon}$ which show patterns of necking bands in the Lagrangian configuration for (a) $\chi^0_{\dot{\varepsilon}} = -0.125$ at $t = 1.656 \cdot 10^{-3}\ s$ and (b) $\chi^0_{\dot{\varepsilon}} = 0.05$ at $t = 1.150 \cdot 10^{-3}\ s$. Initial equivalent loading rate $\dot{\bar{\varepsilon}}^0 = 1000\ s^{-1}$ and isothermal conditions.

In Fig. 9 we show the average Lagrangian band spacing $\bar{L}^{\mathscr{L}}$ obtained by the three methodologies previously described. The abscissa axis is the ratio of strains at diffuse necking $\chi_{\varepsilon}^{neck}$ for methods 1 and 2, and the ratio of strains at perturbation χ_{ε}^{1} for method 3. We already set that the strains corresponding to the condition of diffuse necking in the finite elements may be correlated with the strains corresponding to the condition $\hat{\eta}_{c}^{+} = \boldsymbol{e}$ in the stability analysis, which makes the variables $\chi_{\varepsilon}^{neck}$ and χ_{ε}^{1} comparable *(equivalent)* at some extent. Regarding method 1, for the sake of clarity in the comparison, a fitting curve is used to represent the results obtained using this *(reference)* methodology. The band spacing increases with $\chi_{\varepsilon}^{neck}$ within the whole range of ratios of strain investigated. This trend is consistent with the results of method 2; given the value of the necking strain, the corresponding critical wavenumber calculated with the stability analysis provides an estimation of the band spacing in close agreement with the finite elements. Moreover, when using exclusively the results of the stability analysis (method 3), the predictions find agreement with methods 1 and 2 within the range $-0.15 \leqslant \chi_{\varepsilon}^{1} \leqslant 0.05$. Nevertheless, for $\chi_{\varepsilon}^{1} < -0.15$ and $\chi_{\varepsilon}^{1} > 0.05$, neither the trend nor the values of spacing predicted by method 3 match with the results obtained by methods 1 and 2. Specifically, sufficiently large absolute values of the ratio χ_{ε}^{1} lead to a dramatic decrease in $\bar{L}^{\mathscr{L}}$ with little physical meaning (the average band spacing tends to zero). This drastic decrease is caused by the steep slope displayed by the effective e-instability curve (see Fig. 7) as the absolute value of χ_{ε}^{1} increases. This suggests that, under dynamic loading, the validity of the effective e-instability criterion to predict band spacing may be limited to χ_{ε}^{1} ratios relatively close to plane strain.

Note that the finite element results are obtained under what can be referred to as an *ideal configuration*, in which the perturbation of the field variables necessary to trigger localization is caused by numerical errors intrinsic to the explicit integration of the code. Recall that neither geometric imperfections nor material defects have been used to favour flow localization, the pattern of strain localization is mostly controlled by the dominant instability mode. However, if we would have considered significant material or geometrical defects, the sites of strain localization could have been very much related to such defects. As a function of the interplay between defects (of any type) and the sites of strain localization,

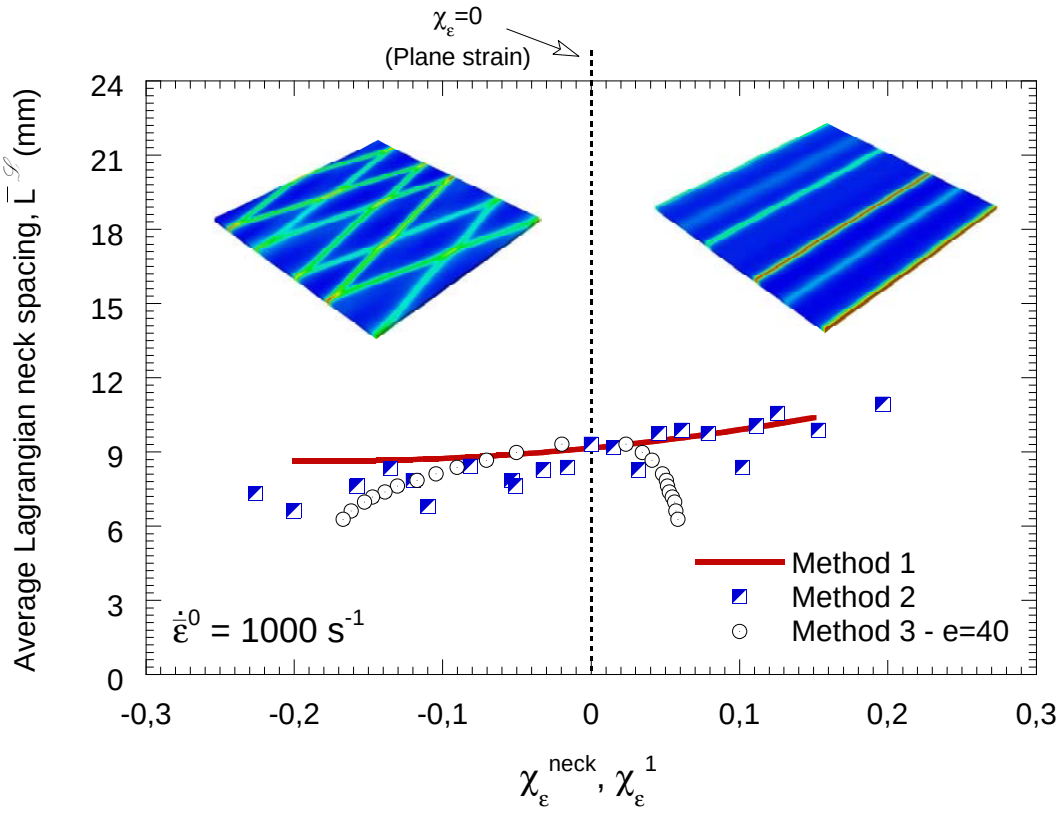

Figure 9: Average Lagrangian band spacing $\bar{L}^{\mathscr{L}}$ obtained from methods 1, 2 and 3. The abscissa axis is the ratio of strain at diffuse necking $\chi_{\varepsilon}^{neck}$ for methods 1 and 2 and the ratio of strains at perturbation χ_{ε}^{1} for method 3. Initial equivalent loading rate $\dot{\bar{\varepsilon}}^{0} = 1000\ s^{-1}$ and isothermal conditions.

we face two different situations:

- Weak interaction between defects and localization sites: it has been found experimentally that multiple (and regular) localization patterns like those presented in this paper can be found in, for instance, dynamic tensile tests performed on steel sheets with a polished surface finish (Vaz-Romero et al., 2015) in which one could assume the absence of significant surface defects. Moreover, the theoretical and numerical results reported for instance by Han and Tvergaard (1995) and Rodríguez-Martínez et al. (2013b) have shown that at very high strain rates (and/or for largely viscid materials) the strain localization pattern is barely related to geometrical and material imperfections, but it is controlled by a dominant mode which determines neck spacing.

- Strong interaction between defects and localization sites: based on a significant number of ring expansion experiments, Zhang and Ravi-Chandar (2006, 2008) showed than under certain loading conditions (strain rates $\lesssim 10^4\ s^{-1}$) and for rate independent metallic materials the defects largely control the necking and fragmentation patterns. This has been further discussed and rationalized for instance by Rodríguez-Martínez et al. (2013c) who showed that defects of large amplitude could dictate the necking pattern, especially if rate independent materials are considered.

Next we will study the effects that loading rate and thermal coupling have on plastic flow localization. Specific attention is paid to the necking band spacing.

6.2. The effect of loading rate

Fig. 10 shows finite element calculations for the diffuse necking strain in principal direction X (ε_x^{neck}) versus the diffuse necking strain in principal direction Y (ε_y^{neck}). Three different loading rates are considered: $\dot{\bar{\varepsilon}}^0 = 500\ s^{-1}$, $\dot{\bar{\varepsilon}}^0 = 1000\ s^{-1}$ (reference) and $\dot{\bar{\varepsilon}}^0 = 5000\ s^{-1}$. It is shown that the necking strain increases with loading rate, for all the loading paths investigated. This is the stabilizing effect of inertia (Fressengeas and Molinari, 1985, 1994; Mercier et al., 2010), which delays the onset of plastic localization.

Fig. 11 shows the average Lagrangian band spacing $\bar{L}^{\mathscr{L}}$ obtained from methods 1, 2 and 3. Two initial equivalent strain rates are investigated: $\dot{\bar{\varepsilon}}^0 = 500\ s^{-1}$ and $\dot{\bar{\varepsilon}}^0 = 5000\ s^{-1}$.

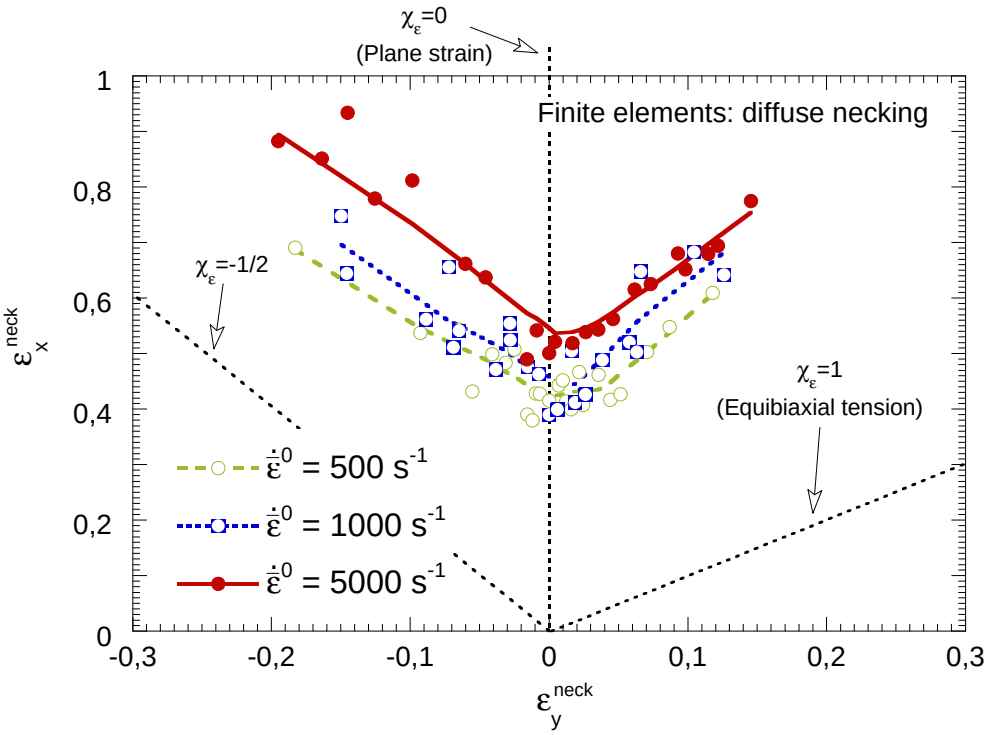

Figure 10: Finite elements: ε_x^{neck} (diffuse necking strain in principal direction X) versus ε_y^{neck} (diffuse necking strain in principal direction Y) for three different initial equivalent strain rates $\dot{\bar{\varepsilon}}^0 = 5000\ s^{-1}$, $\dot{\bar{\varepsilon}}^0 = 1000\ s^{-1}$ (reference) and $\dot{\bar{\varepsilon}}^0 = 500\ s^{-1}$. Isothermal conditions.

Method 1 (finite elements) predicts, irrespective of the loading rate considered, a monotonic rise of the band spacing with increasing $\chi_{\varepsilon}^{neck}$. These trends are properly captured by method 2 (finite elements + stability analysis), which predicts values of neck spacing very similar to those obtained from the finite elements. Method 3, by taking an appropriate value of the effective e-instability, yields results of neck spacing which find agreement with the data obtained from methods 1 and 2 within the range $-0.15 \leqslant \chi_{\varepsilon}^{1} \leqslant 0.05$ in the case of $\dot{\bar{\varepsilon}}^{0} = 500\ s^{-1}$, and within the range $-0.2 \leqslant \chi_{\varepsilon}^{1} \leqslant 0.05$ in the case of $\dot{\bar{\varepsilon}}^{0} = 5000\ s^{-1}$. This suggests that, as we increase the strain rate, the effective e-instability criterion provides better predictions of the neck spacing.

Moreover, it is shown in Fig. 11 that increasing the strain rate markedly shortens the average neck spacing within the whole range of loading paths tested. The strong decrease in neck spacing is consistent with experimental observations and theoretical predictions reported for different loading conditions (Altynova et al., 1996; Grady and Olsen, 2003; Mercier and Molinari, 2003, 2004; Zhang and Ravi-Chandar, 2006; Mercier et al., 2010).

6.3. The effect of thermal coupling

Fig. 12 presents finite element computations for the diffuse necking strain in principal direction X (ε_{x}^{neck}) versus the diffuse necking strain in principal direction Y (ε_{y}^{neck}) considering on the one hand thermal coupling Eq. (16), and on the other hand isothermal conditions (reference). We observe that considering the thermal effects decreases the necking strain and reduces the scatter in the finite element results. The increase of temperature due to plastic deformation is responsible for the early flow localization (Mercier et al., 2010), while the regularizing effect is most likely caused by the thermal conductivity (see the works of Molinari (1997) and Rodríguez-Martínez et al. (2015a)).

Fig. 13 shows the average Lagrangian band spacing $\bar{L}^{\mathscr{L}}$ obtained from methods 1, 2 and 3 considering the thermal coupling. The finite element computations (method 1) predict an increase of the band spacing with increasing $\chi_{\varepsilon}^{neck}$, as in sections 6.1 and 6.2. It is shown by comparison with Fig. 9 (which illustrates the isothermal case), that the thermal effects reduce the neck spacing within the whole range of χ_{ε}^{0} explored. Moreover, to be noted that the results obtained from method 2 (finite elements + stability analysis) are in very good agreement with the finite element computations. On the other hand,

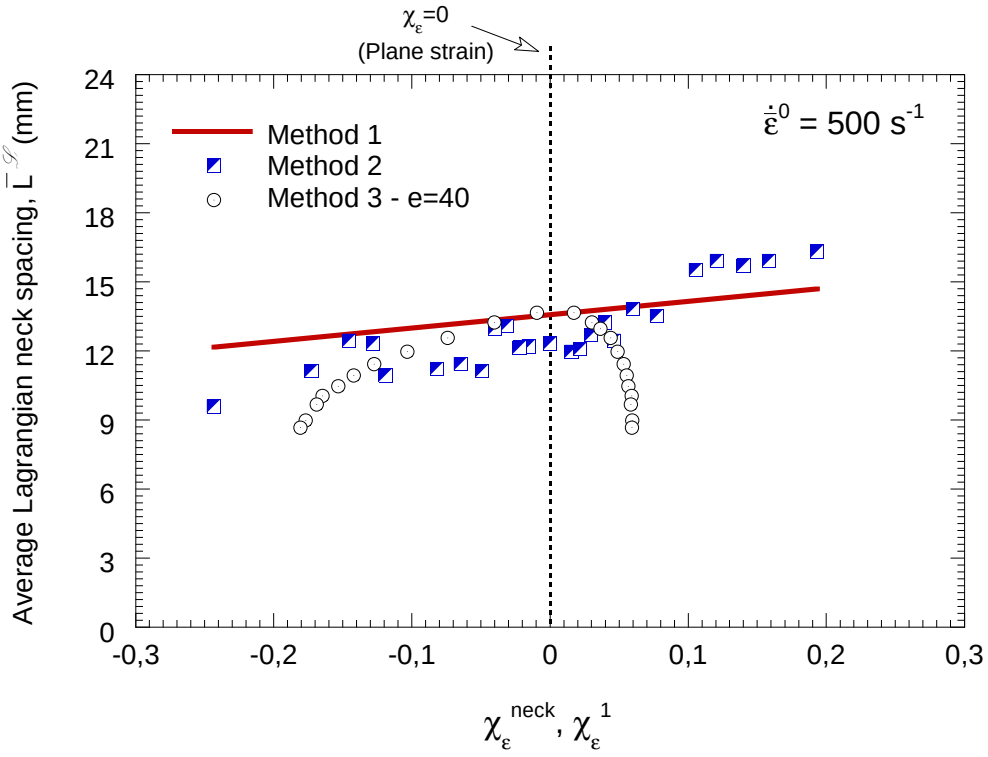

(a)

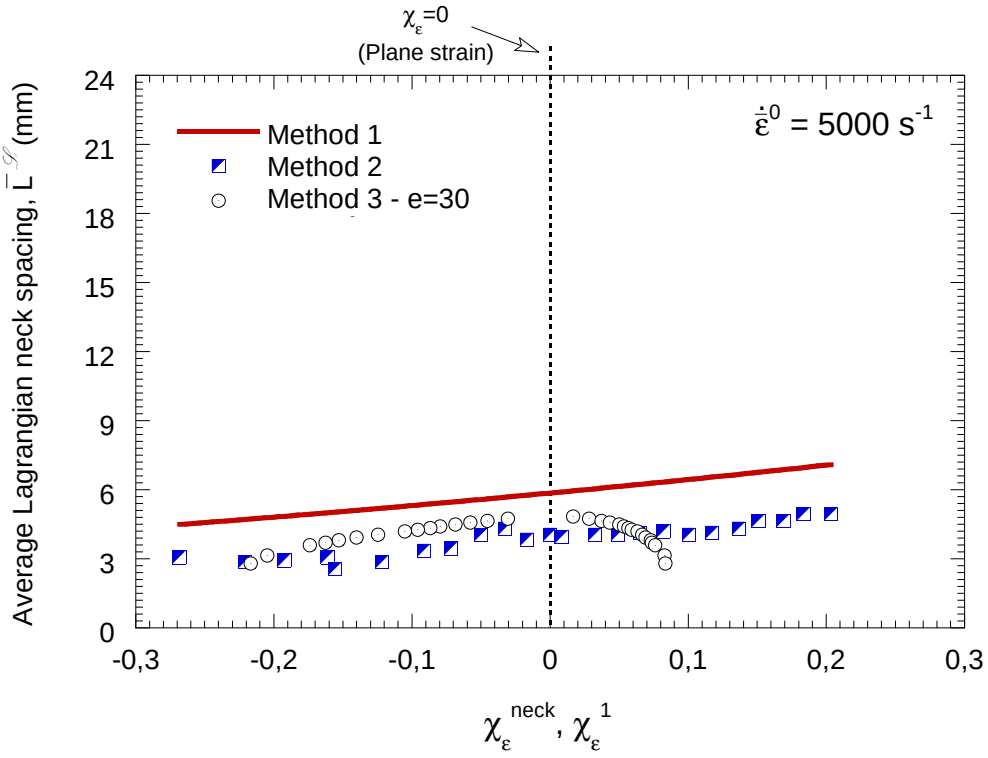

(b)

Figure 11: Average Lagrangian band spacing $\bar{L}^{\mathscr{L}}$ obtained from methods 1, 2 and 3. The abscissa axis is the ratio of strains at diffuse necking $\chi_{\varepsilon}^{neck}$ for methods 1 and 2 and the ratio of strains at perturbation χ_{ε}^{1} for method 3. Two different initial equivalent strain rates are shown: (a) $\dot{\bar{\varepsilon}}^{0} = 500\ s^{-1}$ and (b) $\dot{\bar{\varepsilon}}^{0} = 5000\ s^{-1}$. Isothermal conditions. Results for the reference initial strain rate are shown in Fig. 9.

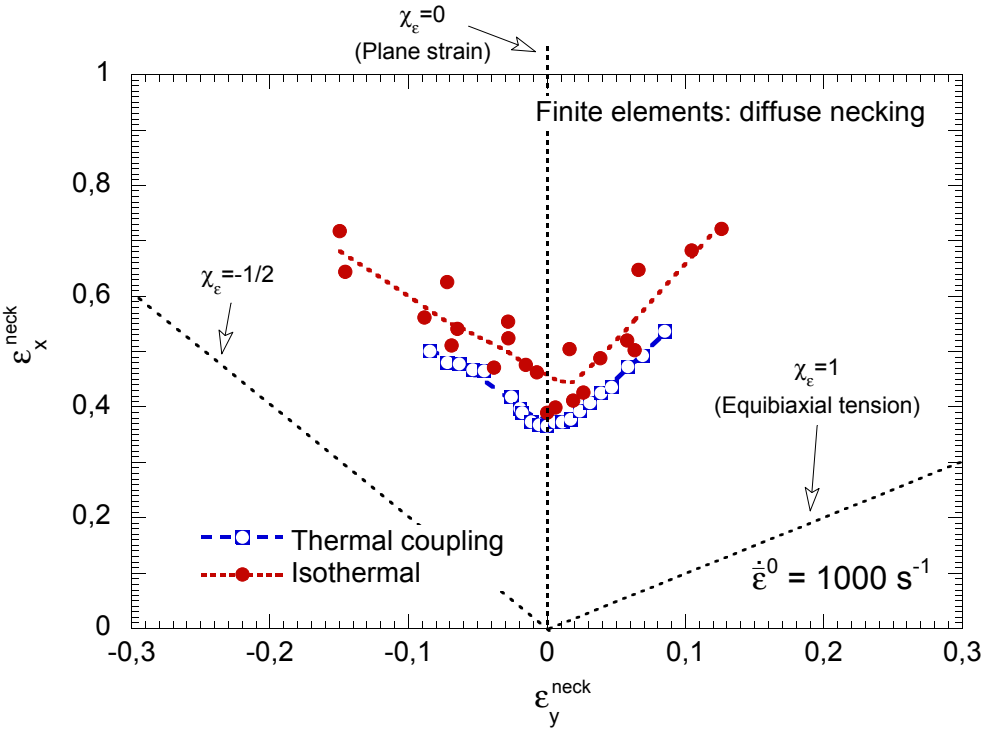

Figure 12: Finite elements: ε_x^{neck} (diffuse necking strain in principal direction X) versus ε_y^{neck} (diffuse necking strain in principal direction Y) considering on the one hand thermal coupling and on the other hand isothermal conditions (reference). Initial equivalent loading rate $\dot{\bar{\varepsilon}}^0 = 1000\ s^{-1}$.

method 3 provides results of neck spacing in agreement with methods 1 and 2 within the range $-0.18 \leqslant \chi_{\varepsilon}^{1} \leqslant 0.05$.

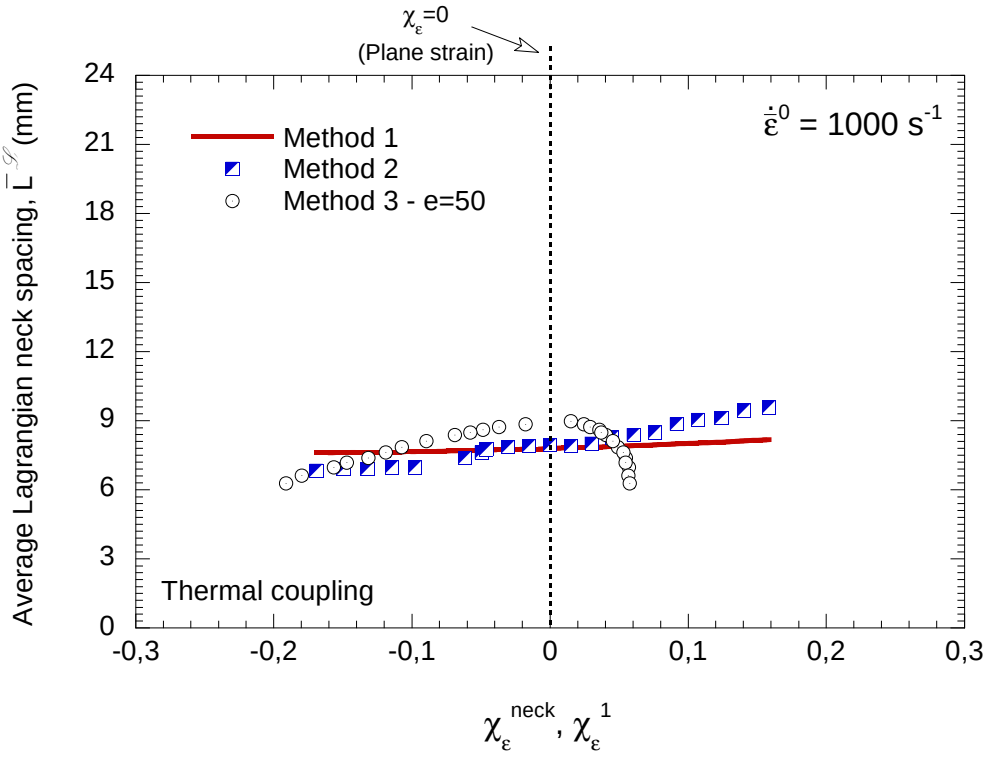

Figure 13: Average Lagrangian band spacing $\bar{L}^{\mathscr{L}}$ obtained from methods 1, 2 and 3 considering the thermal coupling. The abscissa axis is the ratio of strains at diffuse necking $\chi_{\varepsilon}^{neck}$ for methods 1 and 2 and the ratio of strains at perturbation χ_{ε}^{1} for method 3. The thermal coupling is considered. Initial equivalent loading rate $\dot{\bar{\varepsilon}}^{0} = 1000\ s^{-1}$. Results for the isothermal conditions are shown in Fig. 9.

7. Summary and conclusions

In this paper we have investigated the inception and development of necking bands in ductile plates subjected to dynamic (in-plane) biaxial loading. For that task we have developed two different methodologies: (1) a 2D linear stability analysis accounting for stress triaxiality effects, and (2) finite element simulations.

- Linear perturbation analysis: we have extended the original formulation presented by Dudzinski and Molinari (1988, 1991) in order to include inertia and stress triaxiality

effects inside the necking. Inertia slows down the growth of long wavelength perturbations whereas stress triaxiality slows down the growth of short wavelength perturbations. This boosts the growth of an intermediate wavelength which determines the most critical perturbation mode. Relying on this critical mode, we determine the associated critical wavelength and critical directions of perturbation. We have shown that the critical direction of perturbation follows the directions of zero stretch rate if the ratio of strains is negative, whereas it follows the direction of the minor (in plane) principal strain if the ratio of strains is positive.

- Finite element calculations: we have used ABAQUS/Explicit (Simulia, 2013a) to carry out numerical calculations of the problem at hand. In agreement with the stability analysis, the loading conditions correspond to constant velocities applied at the edges of the plate. In order to avoid the spurious propagation of waves along the plate, specific initial conditions consistent with the boundary conditions are imposed. The calculations have shown that multiple necking bands are formed and developed in the plate, following the orientations predicted by the linear stability analysis. Further, the localization patterns predicted by the finite element calculations find good correlation with the experimental evidences reported in the literature by different authors. The simulations performed for $\chi_{\dot{\varepsilon}}^0 < 0$ show the emergence of multiple pairs of bands aligned with the directions of zero stretch rate which intersect at the boundaries of the sample, as shown in the experiments of Vaz-Romero et al. (2015). The simulations performed for $\chi_{\dot{\varepsilon}}^0 \geq 0$ show the development of localization bands parallel to each other (and perpendicular to the major loading direction), as shown in the experiments of Mercier et al. (2010).

The combination of the results obtained from the finite element method and the stability analysis has permitted further insight into the role played by loading path, loading rate and thermal conditions on necking spacing. The following key outcomes have been obtained:

- The effect of loading path: we have measured the distance between localization bands using three different but complementary methodologies. The first method (used as reference) consists on measuring the necks spacing directly from the finite

element computations, the second method combines the results obtained from the finite elements and the stability analysis to determine the average distance between necking bands and the third method (the so-called effective e-instability criterion originally developed by Dudzinski and Molinari (1991)) relies, exclusively, on the stability analysis to predict the distance between bands. Method 2 shows a slight increase of the neck spacing with the ratio of strains, in agreement with finite element calculations (method 1). However, method 3 finds satisfactory agreement with the numerical computations only for negative (up to $\chi_\varepsilon^1 \approx -0.2$) or little positive (up to $\chi_\varepsilon^1 \approx 0.05$) ratios of strain. As a result of the comparison between methods 1 and 2, we can claim that the combination of finite elements and stability analysis is a reliable methodology to predict and rationalize the collective behaviour of the necking bands for all the loading paths explored.

- The effect of loading rate: we have shown that the increase in loading rate leads to the increase of the necking strain for all the loading paths investigated. In principle, this could be in conflict with experimental results recently reported in the literature which showed a decrease in necking strain with increasing applied velocity for certain metallic materials subjected to dynamic biaxial loading. We claim that the trends reported in this paper are intrinsic material effects, while the opposite trends sometimes observed in experiments are primarily caused by structural effects (wave related). Moreover, we have shown that increasing the strain rate markedly shortens the average neck spacing for all the loading paths tested. This observation is consistent with experimental observations and theoretical predictions reported in the literature for different loading conditions.

- The effect of thermal coupling: we have shown that taking into account the thermal coupling leads to a substantial decrease in the necking strain, irrespective of the loading path considered. Further, we have shown that considering the thermal coupling regularizes the finite element computations, most likely because of the role played by thermal conductivity. Moreover, both the linear stability analysis and the numerical calculations demonstrated that the thermal effects shorten the neck spacing.

All in all, in this paper we have developed a detailed theoretical investigation to establish the mechanisms which play a key role in the localization of plastic deformation in ductile plates subjected to dynamic biaxial loading. The systematic confrontation and combination of results obtained from the linear perturbation analysis and the finite element calculations has allowed to provide new insights into the specific localization patterns that emerge under dynamic biaxial loading. As such, we cannot neglect the practical implications that come out from this research. The results presented in this paper may help to devise the definite laboratory tests which are needed to characterize the dynamic failure of sheets subjected to biaxial loading. Further, we claim that this investigation sets a theoretical framework that can be used for design and optimization of high speed metal forming operations, with the ultimate goal of predicting the limits in material ductility which impose important restrictions to this type of industrial processes.

Acknowledgements

JFS, RZ, GV and JARM are indebted to the *Ministerio de Ciencia e Innovación de España* (Projects DPI/2011-24068 and DPI/2011-23191) for the financial support which permitted to conduct this work.

AM and JARM acknowledge the support by the French State through the program Investment in the future operated by the *National Research Agency* (ANR) and referenced by ANR-11-LABX-0008-01 (LabEx DAMAS).

AM acknowledges the support by the University Carlos III de Madrid through the Cátedra de Excelencia funded by Banco Santander.

Appendix A. Kinematics of the fundamental solution

Appendix A.1. Preliminary definitions

- Stretch in the direction given by the unit vector $\boldsymbol{a}$

$$\lambda_a = \frac{d\boldsymbol{x}}{d\boldsymbol{X}} \tag{A.1}$$

with

$$d\boldsymbol{X} = dX\,\boldsymbol{a} \tag{A.2}$$

$$d\boldsymbol{x} = \boldsymbol{F}d\boldsymbol{X} \tag{A.3}$$

and $\boldsymbol{F}$ the deformation gradient.

- Logarithmic deformation in direction $\boldsymbol{a}$

$$\varepsilon_a = \ln\lambda_a \tag{A.4}$$

- Rate of deformation in direction $\boldsymbol{a}$

$$\frac{D\varepsilon_a}{Dt} = \boldsymbol{a}^T\boldsymbol{d}\,\boldsymbol{a} \tag{A.5}$$

$\boldsymbol{d}$ being the rate of deformation tensor.

Appendix A.2. Formulation in the frame $\{X, Y\}$

For direction x we assume a linear variation of velocity with the Lagrangian coordinate X

$$V_x = \frac{DU_x}{Dt} = \dot{\varepsilon}_x^0 X \tag{A.6}$$

$\dot{\varepsilon}_x^0$ being a constant. This velocity field leads to a null acceleration

$$A_x = \frac{DV_x}{Dt} = 0 \tag{A.7}$$

which guarantees a uniform stress field for the fundamental solution. Displacement is obtained by temporal integration

$$U_x = \dot{\varepsilon}_x^0 X t \tag{A.8}$$

and the Eulerian coordinate is given by

$$x = X + U_x = \left(1 + \dot{\varepsilon}_x^0 t\right) X \tag{A.9}$$

The logarithmic strain and strain rate (material time derivative of strain) are given by

$$\varepsilon_x = ln\left(\frac{\partial x}{\partial X}\right) = ln\left(1 + \dot{\varepsilon}_x^0 t\right) \tag{A.10}$$

$$\dot{\varepsilon}_x = \frac{\dot{\varepsilon}_x^0}{1 + \dot{\varepsilon}_x^0 t} \tag{A.11}$$

In Eulerian coordinates the velocity is

$$v_x = \frac{\dot{\varepsilon}_x^0}{1 + \dot{\varepsilon}_x^0 t} x \tag{A.12}$$

and the rate of deformation

$$d_{xx} = \frac{\partial v_x}{\partial x} = \frac{\dot{\varepsilon}_x^0}{1 + \dot{\varepsilon}_x^0 t} \tag{A.13}$$

We may proceed in the same way for direction y

$$V_y = \frac{DU_y}{Dt} = \dot{\varepsilon}_y^0 Y \tag{A.14}$$

$$y = Y + U_y = \left(1 + \dot{\varepsilon}_y^0 t\right) Y \tag{A.15}$$

$$\varepsilon_y = ln\left(1 + \dot{\varepsilon}_y^0 t\right) \tag{A.16}$$

$$\dot{\varepsilon}_y = \frac{\dot{\varepsilon}_y^0}{1 + \dot{\varepsilon}_y^0 t} \tag{A.17}$$

$$v_y = \frac{\dot{\varepsilon}_y^0}{1 + \dot{\varepsilon}_y^0 t} y \tag{A.18}$$

$$d_{yy} = \frac{\partial v_y}{\partial y} = \frac{\dot{\varepsilon}_y^0}{1 + \dot{\varepsilon}_y^0 t} \tag{A.19}$$

As can be observed in previous equations, the requirement of uniformity in the stress field leads to a non-proportional straining path

$$\frac{d_{yy}}{d_{xx}} \neq constant \; ; \qquad \frac{\varepsilon_y}{\varepsilon_x} \neq constant \tag{A.20}$$

Nevertheless, note that the variation of previous ratios upon the loading is almost negligible for the loading cases analysed in this paper, as previously shown in Fig. 4.

Regarding direction z we use the incompressibility condition $\mathrm{tr}\,(\boldsymbol{d}) = 0$ to get

$$d_{zz} = -\frac{\dot{\varepsilon}_x^0}{1 + \dot{\varepsilon}_x^0 t} - \frac{\dot{\varepsilon}_y^0}{1 + \dot{\varepsilon}_y^0 t} \tag{A.21}$$

Integrating Eq. (A.21) in z

$$v_z = \left(-\frac{\dot{\varepsilon}_x^0}{1 + \dot{\varepsilon}_x^0 t} - \frac{\dot{\varepsilon}_y^0}{1 + \dot{\varepsilon}_y^0 t}\right) z \tag{A.22}$$

Integrating Eq. (A.21) in t and taking into account $\dot{\varepsilon}_z = d_{zz}$ (Eq. (A.5))

$$\varepsilon_z = ln\left(\frac{1}{\left(1 + \dot{\varepsilon}_x^0 t\right)\left(1 + \dot{\varepsilon}_y^0 t\right)}\right) \tag{A.23}$$

and from the definition of ε_z

$$\varepsilon_z = ln\left(\frac{\partial z}{\partial Z}\right) \tag{A.24}$$

we get

$$z = \frac{Z}{(1+\dot{\varepsilon}_x^0 t)\left(1+\dot{\varepsilon}_y^0 t\right)} \tag{A.25}$$

Finally, the deformation gradient is

$$\boldsymbol{F} = \begin{pmatrix} 1+\dot{\varepsilon}_x^0 t & 0 & 0 \\ 0 & 1+\dot{\varepsilon}_y^0 t & 0 \\ 0 & 0 & \frac{1}{(1+\dot{\varepsilon}_x^0 t)\left(1+\dot{\varepsilon}_y^0 t\right)} \end{pmatrix} \tag{A.26}$$

and the rate of deformation tensor

$$\boldsymbol{d} = \mathrm{sym}\left(\boldsymbol{l}\right) = \mathrm{sym}\left(\dot{\boldsymbol{F}}\boldsymbol{F}^{-1}\right) = \begin{pmatrix} d_{xx} & 0 & 0 \\ 0 & d_{yy} & 0 \\ 0 & 0 & -\left(d_{xx}+d_{yy}\right) \end{pmatrix} \tag{A.27}$$

$\boldsymbol{l}$ being the velocity gradient. The proposed kinematics is homogeneous, deformation gradient is not a function of the reference coordinates, therefore it carries straight lines into straight lines. Considering a straight necking band in the reference configuration, given by its angle $\Omega^{\mathscr{L}} = \Psi + \pi/2$ with respect to X axis, it is useful to know its orientation in the deformed configuration, given by the angle $\Omega^{\mathscr{E}}$

$$\Omega^{\mathscr{E}} = \arctan\left(\frac{1+\dot{\varepsilon}_y^0 t}{1+\dot{\varepsilon}_x^0 t}\,\tan\,\Omega^{\mathscr{L}}\right) \tag{A.28}$$

Appendix A.3. Formulation in the frame $\{X_1, X_2\}$

Velocities are given by

$$v_1 = \frac{\dot{\varepsilon}_x^0 x}{1+\dot{\varepsilon}_x^0 t}\cos\Psi + \frac{\dot{\varepsilon}_y^0 y}{1+\dot{\varepsilon}_y^0 t}\sin\Psi \tag{A.29}$$

$$v_2 = \frac{\dot{\varepsilon}_y^0 y}{1+\dot{\varepsilon}_y^0 t}\cos\Psi - \frac{\dot{\varepsilon}_x^0 x}{1+\dot{\varepsilon}_x^0 t}\sin\Psi \tag{A.30}$$

rates of deformations by

$$d_{11} = \frac{\dot{\varepsilon}_x^0}{1+\dot{\varepsilon}_x^0 t}\cos^2\Psi + \frac{\dot{\varepsilon}_y^0}{1+\dot{\varepsilon}_y^0 t}\sin^2\Psi \tag{A.31}$$

$$d_{22} = \frac{\dot{\varepsilon}_y^0}{1+\dot{\varepsilon}_y^0 t}\cos^2\Psi + \frac{\dot{\varepsilon}_x^0}{1+\dot{\varepsilon}_x^0 t}\sin^2\Psi \tag{A.32}$$

$$d_{12} = \frac{-\dot{\varepsilon}_x^0 + \dot{\varepsilon}_y^0}{\left(1+\dot{\varepsilon}_x^0 t\right)\left(1+\dot{\varepsilon}_y^0 t\right)}\cos\Psi\sin\Psi \tag{A.33}$$

$$\boldsymbol{d} = \begin{pmatrix} d_{11} & d_{12} & 0 \\ d_{12} & d_{22} & 0 \\ 0 & 0 & -\left(d_{11}+d_{22}\right) \end{pmatrix} \tag{A.34}$$

and the deformation gradient by

$$\boldsymbol{F} = \begin{pmatrix} \left(1+\dot{\varepsilon}_x^0 t\right)\cos^2\Psi + \left(1+\dot{\varepsilon}_y^0 t\right)\sin^2\Psi & \left(-\dot{\varepsilon}_x^0 + \dot{\varepsilon}_y^0\right) t\ \cos\Psi\sin\Psi & 0 \\ \left(-\dot{\varepsilon}_x^0 + \dot{\varepsilon}_y^0\right) t\ \cos\Psi\sin\Psi & \left(1+\dot{\varepsilon}_y^0 t\right)\cos^2\Psi + \left(1+\dot{\varepsilon}_x^0 t\right)\sin^2\Psi & 0 \\ 0 & 0 & \frac{1}{\left(1+\dot{\varepsilon}_x^0 t\right)\left(1+\dot{\varepsilon}_y^0 t\right)} \end{pmatrix} \tag{A.35}$$

Appendix B. Stress correction in the neck due to stress triaxiality for a general biaxial state

Consider a sheet with a neck aligned to direction 2 and submitted to a remote biaxial stress state in directions 1 and 2. The neck has a thickness $2a$ and its contour has a radius

of curvature R. Following the theory of Bridgman (1952), we may assume that the stress field across the neck σ_{ij}^{neck} consists of a uniform field σ_{ij}^{u} plus a superposed hydrostatic stress σ_h which may vary with the coordinate z

$$\sigma_{ij}^{neck}(z) = \sigma_{ij}^{u} + \sigma_h(z) \qquad \text{for } i = j \tag{B.1}$$

$$\sigma_{ij}^{neck}(z) = 0 \qquad \text{for } i \neq j \tag{B.2}$$

We may use the expression proposed by Bridgman for the stress distribution in the out-of-plane direction

$$\sigma_{33}^{neck}(z) = \sigma_{11}^{a} f(z) \tag{B.3}$$

σ_{11}^{a} being the stress σ_{11}^{neck} at $z = a$, and

$$f(z) = \log\left[1 + \frac{1}{2}\frac{a}{R}\left(1 - \frac{z^2}{a^2}\right)\right] \tag{B.4}$$

This expression was derived for plane strain ($\varepsilon_{22} = 0$) and plane stress ($\sigma_{22} = 0$) conditions but it is likewise valid for any other strain or stress condition in direction 2 since it just denotes equilibrium in the out-of-plane direction.

Following Bridgman, we may assume that the constant stress in direction z is $\sigma_{33}^{u} = 0$. Then

$$\sigma_h(z) = \sigma_{33}^{neck}(z) = \sigma_{11}^{a} f(z) \tag{B.5}$$

and

$$\sigma_{11}^{neck}(z) = \sigma_{11}^{u} + \sigma_{11}^{a} f(z) \tag{B.6}$$

Given that $f(a) = 0$, then $\sigma_{11}^{a} = \sigma_{11}^{u}$. We may now obtain the averaged stresses along the neck in direction 1

$$\sigma_{11}^{avg} = \frac{\int_0^a \sigma_{11}^{neck}(z)\, dz}{a} = \sigma_{11}^{u} B_1(\phi) \tag{B.7}$$

where

$$B_1(\phi) = \sqrt{1+\phi^{-1}} \log\left(1 + 2\phi + 2\sqrt{\phi(1+\phi)}\right) - 1 \tag{B.8}$$

with

$$\phi = \frac{a}{2R} = \frac{h}{8}\frac{\partial^2 h}{\partial x_1^2} \tag{B.9}$$

This factor relating constant and averaged values of the stress σ_{11}^{neck} was derived by Bridgman for plane strain or plane stress conditions in direction 2 and, as stated here, is equally valid for any other biaxial state.

Eq. (B.7) provides the relation between averaged and constant values of the stress in direction 1 which has been validated with a finite element model, developed with ABAQUS/Standard (Simulia, 2013b), for three different ratios of strain $\varepsilon_{22}/\varepsilon_{11}$ namely uniaxial tension, plane strain and equibiaxial stretching. Five different values of ϕ were considered, consistent with those adopted by Bai et al. (2009) for plane strain conditions. The results presented in Fig. B.1 show the validity of Eq. (B.7) to relate averaged and uniform stress in direction for the $\varepsilon_{22}/\varepsilon_{11}$ range of interest in forming analysis.

In regard to the usage of the previous approach to consider the neck triaxiality effects in the governing equations (Section 2) and linear stability analysis (Section 3), it is worth to state the following remarks:

- Averaged values of the stresses should be used for the momentum equations.
- Since the hydrostatic component σ_h does not affect neither yield nor plastic flow, uniform values of the stresses should be used in both yield condition and flow rule. Likewise, they should be used to calculate the plastic work.

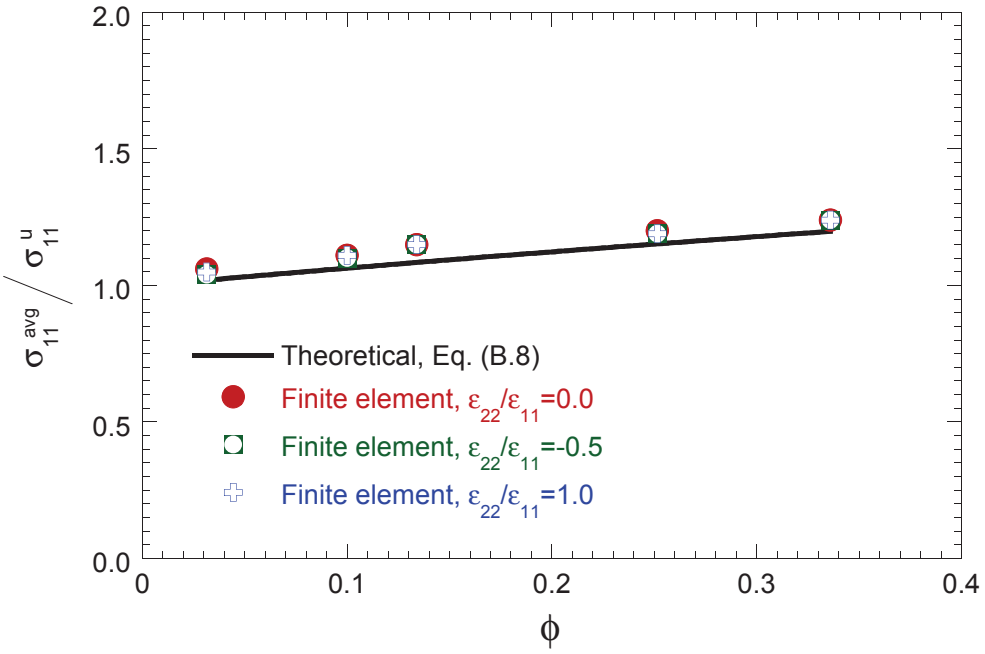

Figure B.1: Validation of the Bridgman correction factor $B_1(\phi)$ (Eq. (B.8)) for equibiaxial stretching, plane strain and uniaxial tension.

- The correction factor B_1 has been derived for a biaxial stress state, thus neglecting remote shear stresses, in order to fulfill the hypothesis and equations of the analysis proposed by Bridgman (principal stresses along the three coordinate axes). For simplicity, we may however consider this factor in the more general case of a stress state including σ_{12}. In this case, we do not establish any difference between averaged and constant values of the shear stress, that is, $\sigma_{12}^{neck} = \sigma_{12}^{avg} = \sigma_{12}$.

Appendix C. Spatial derivation of a perturbation in a 2D Lagrangian frame

Perturbation of Eqs. (1-3), (14-16) and (18) requires the inverse of the perturbed deformation gradient in the frame $\{X_1, X_2\}$. Starting from the perturbation of the Eulerian coordinates

$$x_1 = x_1^1 + \Delta x_1 = x_1^1 + \delta x_1 e^{i\xi X_1} e^{\eta(t-t^1)} \tag{C.1}$$

$$x_2 = x_2^1 + \Delta x_2 = x_2^1 + \delta x_2 e^{i\xi X_1} e^{\eta(t-t^1)} \tag{C.2}$$

the perturbed deformation gradient (considering only the components in the sheet plane) becomes

$$\boldsymbol{F}_{2D} = \begin{pmatrix} F^1_{11} + i\xi\Delta x_1 & F^1_{12} \\ F^1_{21} + i\xi\Delta x_2 & F^1_{22} \end{pmatrix} \tag{C.3}$$

and its inverse

$$\boldsymbol{F}^{-1}_{2D} = \frac{1}{\Lambda} \begin{pmatrix} F^1_{22} & -F^1_{12} \\ -F^1_{21} - i\xi\Delta x_2 & F^1_{11} + i\xi\Delta x_1 \end{pmatrix} \tag{C.4}$$

with

$$\Lambda = \det(\boldsymbol{F}_{2D}) = F^1_{11}F^1_{22} - F^1_{12}F^1_{21} - i\xi F^1_{12}\Delta x_2 + i\xi F^1_{22}\Delta x_1 \tag{C.5}$$

Then, derivatives of the increment of a generic variable Δf with respect to x_1 or x_2 are calculated as

$$\frac{\partial \Delta f}{\partial x_1} = \frac{\partial \Delta f}{\partial X_1}\frac{\partial X_1}{\partial x_1} = i\xi\Delta f\frac{F^1_{22}}{\Lambda} \tag{C.6}$$

$$\frac{\partial \Delta f}{\partial x_2} = \frac{\partial \Delta f}{\partial X_1}\frac{\partial X_1}{\partial x_2} = -i\xi\Delta f\frac{F^1_{12}}{\Lambda} \tag{C.7}$$

Multiplying the linearized equations by Λ and neglecting higher order terms will preserve only the factor $\Lambda^1 = F^1_{11}F^1_{22} - F^1_{12}F^1_{21}$. Thus Λ is approximated by Λ^1, and δx_1 and δx_2 do not appear in the resulting Eqs. (C.6) and (C.7).

Appendix D. Diffuse and localized necking criteria

We evaluate material instability using both diffuse and localized necking criteria. As in section 6, we use the reference material parameters listed in Table 3 and the analysis is conducted under isothermal conditions ($\beta = 0$) for the initial loading rate $\dot{\bar{\varepsilon}}^0 = 1000\ s^{-1}$.

Following the procedure reported elsewhere (Triantafyllidis and Waldenmyer, 2004; Xue et al., 2008; Rodríguez-Martínez et al., 2013c,b), the localized necking strain is given by the condition $d\bar{\varepsilon}/dt = 0$, where $\bar{\varepsilon}$ is measured within the unloading zone which surrounds the necking band. The term localized necking describes the stage of the loading process for which plastic flow is fully concentrated in the necked region.

Fig. D.2 shows the necking strain in principal direction X versus the necking strain in principal direction Y corresponding to diffuse and localized necking conditions. It is observed that the scatter in the measurement of the necking strain (solid points) is substantially reduced using the criterion of localized necking. This is a robust criterion, less influenced by the variability in the round-off errors of the finite element code than the diffuse necking criterion. However, the $\varepsilon_x^{neck} - \varepsilon_y^{neck}$ curves corresponding to both criteria are very similar in shape, the only difference is that the results corresponding to the localized criterion are shifted upwards. This reinforces the idea introduced in section 6, for a sufficiently large number of finite element results the diffuse necking criterion provides consistent trends in the ε_x^{neck} - ε_y^{neck} graph, in agreement with the results obtained from the commonly used localized necking criterion.

References

Aboutalebi, F., Farzin, M., Mashayekhi, M., 2012. Numerical predictions and experimental validations of ductile damage evolution in sheet metal forming processes. Acta Mechanica Solida Sinica 25, 638–649.

Altynova, M., Hu, X., Daehn, G. S., 1996. Increased ductility in high velocity electromagnetic ring expansion. Metall Trans A 27, 1837–1844.

Bai, Y., Teng, X., Wierzbicki, T., 2009. On the Application of Stress Triaxiality Formula for Plane Strain Fracture Testing. Journal of Engineering Materials and Technology 131, 021002–1.

Bai, Y., Wierzbicki, T., 2010. Application of extended Mohr-Coulomb criterion to ductile fracture. International Journal of Fracture 161, 1–20.

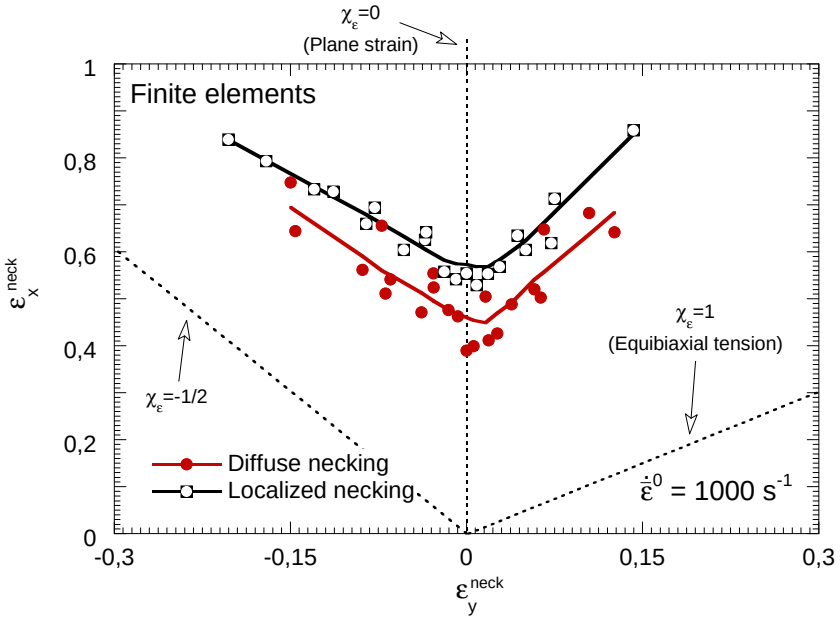

Figure D.2: Finite elements. Necking strain in principal direction X $\left(\varepsilon_x^{neck}\right)$ versus necking strain in principal direction Y $\left(\varepsilon_y^{neck}\right)$ corresponding to diffuse and localized necking conditions. Material parameters listed in Table 3, isothermal conditions $\beta = 0$ and initial loading rate $\dot{\bar{\varepsilon}}^0 = 1000\ s^{-1}$.

Bai, Y. L., 1982. Thermo-plastic instability in simple shear. Journal of the Mechanics and Physics of Solids 30, 195–207.

Barata da Rocha, A., Barlat, F., Jalinier, J., 1985. Prediction of the forming limit diagrams of anisotropic sheets in linear and non-linear loading. Materials Science and Engineering 68, 151–164.

Bridgman, P. W., 1952. Studies in large plastic flow and fracture, with special emphasis on the effects of hydrostatic pressure, vol.1. McGraw-Hill Book Company, Inc., New York.

Chen, J., Zhou, X., Chen, J., 2010. Sheet metal forming limit prediction based on plastic deformation energy. Journal of Materials Processing Technology 210, 315–322.

Chin-Chan, C., 1995. An investigation of the strain path dependence of the forming limit curve. International Journal of Solids and Structures 18, 205–215.

Clift, S., Hartley, P., Sturgess, C., Rowe, G., 1990. Fracture prediction in plastic deformation processes. International Journal of Mechanical Sciences 32, 1–17.

Clifton, R., Duffy, J., Hartley, K. W., Shawki, T. G., 1984. On critical conditions for shear band formation at high strain rates. Scripta Metallurgica 18, 443–448.

Cockcroft, M., Latham, D., 1968. Ductility and the workability of metals. Journal of the Institute of Metals 96, 33–39.

Dudzinski, D., Molinari, A., 1988. Instability of visco-plastic deformation in biaxial loading. Comptes Rendues Academie Science Paris 307, 1315–1321.

Dudzinski, D., Molinari, A., 1991. Perturbation analysis of thermoviscoplastic instabilities in biaxial loading. International Journal of Solids and Structures 27, 601–628.

Fressengeas, C., Molinari, A., 1985. Inertia and thermal effects on the localization of plastic flow. Acta Metallurgica 33, 387–396.

Fressengeas, C., Molinari, A., 1994. Fragmentation of rapidly stretching sheets. European Journal of Mechanics A/Solids 13, 251–268.

Goodwin, G., 1968. Application of strain analysis to sheet metal forming problems in the press shop. SAE Technical Paper No. 680093.

Grady, D. E., Olsen, M. L., 2003. A statistics and energy based theory of dynamic fragmentation. International Journal of Impact Engineering 29, 293–306.

Graf, A., Hosford, W., 1990. Calculations of forming limit diagrams. Metallurgical Transactions A 21, 87–93.

Grolleau, V., Gary, G., Mohr, D., 2008. Biaxial testing of sheet materials at high strain rates using viscoelastic bars. Experimental Mechanics 48, 293–306.

Gurson, A., 1977. Continuum theory of ductile rupture by void nucleation and growth. Part I: Yield criteria and flow rules for porous ductile media. ASME Journal of Engineering Materials and Technology 99, 2–15.

Han, H., Kim, K., 2003. A ductile fracture criterion in sheet metal forming process. Journal of Materials Processing Technology 142, 231–238.

Han, J. B., Tvergaard, V., 1995. Effect of inertia on the necking behaviour of ring specimens under rapid axial expansion. European Journal of Mechanics A/Solids 14, 287–307.

Hill, R., 1952. On discontinous plastic states, with special reference to localized necking in thin sheets. Journal of the Mechanics and Physics of Solids 1, 19–30.

Hutchinson, J. W., Neale, K., Needleman, A., 1978. Mechanics of sheet metal forming. Plenum Press, New York/London, pp. 269–285.

Jie, M., Cheng, C., Chan, L., Chow, C., 2009. Forming limit diagrams of strain-rate dependent sheet metals. International Journal of Mechanical Sciences 51, 269–275.

Jouve, D., 2013a. Analytic study of plastic necking instabilities during plane tension tests. European Journal of Mechanics A/Solids 39, 180–196.

Jouve, D., 2013b. Analytic study of the onset of plastic instabilities during plane tension and compression tests on metallic plates. European Journal of Mechanics A/Solids 47, 70–81.

Keeler, S., Backofen, W., 1963. Plastic instability and fracture in sheets stretched over rigid punches. Transactions of American Society for Metals 56, 25–48.

Ko, Y., Lee, J., Huh, H., Kim, H., Park, S.-H., 2007. Prediction of fracture in hubhole expanding process using a new ductile fracture criterion. Journal of Materials Processing Technology 187, 358–362.

Krajcinovic, D., Lemaitre, J., 1987. Continuum Damage Mechanics: Theory and Applications. Springer, Berlin.

Lee, D., Zaverl, F., 1982. Necking growth and forming limits in sheet metals. International Journal of Mechanical Sciences 24, 157–173.

Lee, Y., Kwon, Y., Kang, S., Kim, S., Lee, J., 2008. Forming limit of AZ31 alloy sheet and strain rate on warm sheet metal forming. Journal of Materials Processing Technology 201, 431–435.

Lemaitre, J., 1993. A three-dimensional ductile damage model applied to deep-drawing forming limits. In: Canlsson, J., Ohlson, N. (Eds.), Mechanical Behaviour of Materials–IV, Proc. ICM-4. Pergamon Press, Oxford, pp. 659–665.

Lemaitre, L., Chaboche, J. L., 1990. Mechanics of Solid Materials. Cambridge University Press, Cambridge.

Li, M., Chandra, A., 1999. Influence od strain-rate sensitivity on necking and instability in sheet metal forming. Journal of the Materials Processing Technology 96, 133–138.

Li, M., Zhu, X., Chu, E., 2012. Effect of strain rate sensitivity on FLDs–An instability approach. International Journal of Mechanical Sciences 64, 273–279.

Liu, H., Yang, Y., Yu, Z., Sun, Z., Wang, Y., 2009. The application of a ductile fracture criterion to the prediction of the forming limit of sheet metals. Journal of Materials Processing Technology 209, 5443–5447.

Lou, Y., Huh, H., Lim, S., Pack, K., 2012. New ductile fracture criterion for prediction of fracture forming limit diagrams of sheet metals. International Journal of Solids and Structures 49, 3605–3615.

Marciniak, Z., Kuckzynski, K., 1967. Limit strains in the process of stretch-forming sheet metal. International Journal of Mechanical Sciences 9, 609–620.

Mercier, S., Granier, N., Molinari, A., Llorca, F., Buy, F., 2010. Multiple necking during the dynamic expansion of hemispherical metallic shells, from experiments to modelling. Journal of the Mechanics and Physics of Solids 58, 955–982.

Mercier, S., Molinari, A., 2003. Predictions of bifurcations and instabilities during dynamic extensions. International Journal of Solids and Structures 40, 1995–2016.

Mercier, S., Molinari, A., 2004. Analysis of multiple necking in rings under rapid radial expansion. International Journal of Impact Engineering 30, 403–419.

Molinari, A., 1985. Instabilité thermoviscoplastique en cisaillement simple. Journal de Mécanique Théorique et Appliquée 4, 659–684.

Molinari, A., 1997. Collective behaviour and spacing of adiabatic shear bands. Journal of the Mechanics and Physics of Solids 45, 1551–1575.

Molinari, A., Clifton, R., 1987. Analytical characterization of shear localization in themoviscoplastic materials. Journal of Applied Mechanics 54, 806–812.

Needleman, A., Rice, J., 1978. Limits to Ductility Set by Plastic Flow Localization. Mechanics of Sheet Metal Forming. Plenum Press, pp. 137–267.

Nie, Q., Lee, D., 1991. The effect of rate-sensitivity on history dependent forming limit of anisotropic sheet metals. Journal of Materials Shaping Technology 9, 233–240.

Novak, J., Laurova, D., 1989. Bifurcation analysis of localized necking in thin sheets and prediction of fracture strains. Acta Technica Csav 34, 525–536.

Oh, S., Chen, C., Kobayashi, S., 1979. Ductile fracture in axisymmetric extrusion and drawing: Part 2, workability in extrusion and drawing. ASME Journal of Engineering for Industry 101, 36–44.

Oliveira, D., Worswick, M., Finn, M., Newman, D., 2005. Electromagnetic forming of aluminium alloy sheet: free-form and cavity fill experiments and model. Journal of Materials Processing Technology 170, 350–362.

Oyane, M., Sato, T., Okimoto, K., Shima, S., 1980. Criteria for ductile fracture and their applications. Journal of Mechanical Working Technology 4, 65–81.

Ozturk, F., Lee, D., 2004. Analysis of forming limits using ductile fracture criteria. Journal of Materials Processing Technology 147, 397–404.

Percy, J., 1980. The effect of strain rate on the FLD for sheet metal. Annals of the CIRP 29, 151–152.

Ramezani, M., Ripin, Z., 2010. Combined experimental and numerical analysis of bulge test at high strain rates using split Hopkinson pressure bar apparatus. Journal of Materials Processing Technology 201, 1061–1069.

Rodríguez-Martínez, J. A., Rittel, D., Zaera, R., Osovski, S., 2013a. Finite element analysis of AISI 304 steel sheets subjected to dynamic tension: the effects of martensitic transformation and plastic strain development on flow localization. International Journal of Impact Engineering 53, 206–216.

Rodríguez-Martínez, J. A., Vadillo, G., Fernández-Sáez, J., Molinari, A., 2013b. Identification of the critical wavelength responsible for the fragmentation of ductile rings expanding at very high strain rates. Journal of the Mechanics and Physics of Solids 61, 1357–1376.

Rodríguez-Martínez, J. A., Vadillo, G., Rittel, D., Zaera, R., Fernández-Sáez, J., 2015a. Dynamic recrystallization and adiabatic shear localization. Mechanics of Materials 81, 41–55.

Rodríguez-Martínez, J. A., Vadillo, G., Zaera, R., Fernández-Sáez, J., 2013c. On the complete extinction of selected imperfection wavelengths in dynamically expanded ductile rings. Mechanics of Materials 60, 107–120.

Rodríguez-Martínez, J. A., Vadillo, G., Zaera, R., Fernández-Sáez, J., Rittel, D., 2015b. An analysis of microstructural and thermal softening effects in dynamic necking. Mechanics of Materials 80, 298–310.

Rusinek, A., Zaera, R., 2007. Finite element simulation of steel ring fragmentation under radial expansion. International Journal of Impact Engineering 34, 799–822.

Seth, M., Vohnout, V., Daehn, G., 2005. Formability of steel in high velocity impact. Journal of Materials Processing Technology 168, 390–400.

Shimamoto, A., Shimomura, T., Nam, J., 2003. The development of servo dynamic biaxial loading device. Key Engineering Materials 243–244, 99–104.

Simulia, 2013a. ABAQUS/Explicit User's Manual, version 6.13 Edition. Dassault Systèmes, Providence, USA.

Simulia, 2013b. ABAQUS/Standard User's Manual, version 6.13 Edition. Dassault Systèmes, Providence, USA.

Stören, S., Rice, J., 1975. Localized necking in thin sheets. Journal of the Mechanics and Physics of Solids 23, 421–441.

Swift, H., 1952. Plastic instability under plane stress. Journal of the Mechanics and Physics of Solids 1, 1–18.

Tai, W., 1985. A damage mechanics model for anisotropic materials and its application to sheet metal forming. International Journal of Solids and Structures 24, 1045–1057.

Takuda, H., Mori, K., Hatta, N., 1999. The application of some criteria for ductile fracture to the prediction of the forming limit of sheet metals. Journal of Materials Processing Technology 95, 116–121.

Toth, L., Dudzinski, D., Molinari, A., 1996. Forming limit predictions with the perturbation method using stress potential functions of polycrystal visco-plasticity. International Journal of Mechanical Sciences 38, 805–824.

Triantafyllidis, N., Waldenmyer, J. R., 2004. Onset of necking in electro-magnetically formed rings. J Mech Phys Solids 52, 2127–2148.

Tvergaard, V., Needleman, A., 1984. Analysis of the cup-cone fracture in a round tensile bar. Acta Metallurgica 32, 157–169.

Vadillo, G., Rodríguez-Martínez, J. A., Fernández-Sáez, J., 2012. On the interplay between strain rate and strain rate sensitivity on flow localization in the dynamic expansion of ductile rings. International Journal of Solids and Structures 49, 481–491.

Vaz-Romero, A., Rodríguez-Martínez, J. A., Arias, A., 2015. The deterministic nature of the fracture location in the dynamic tensile testing of steel sheets. International Journal of Impact Engineering doi:10.1016/j.ijimpeng.2015.08.005.

Verleysen, P., Peirs, J., Van Slycken, J., Faes, K., Duchene, L., 2011. Effect of strain rate on the forming behaviour of sheet metals. Journal of Materials Processing Technology 211, 1457–1464.

Wang, T., 1995. Prediction of sheet forming limits using a new continuum damage mechanics criterion for ductile fracture. Engineering Fracture Mechanics 51, 275–279.

Wifi, A., Adbel-Hamed, A., El-Abbasi, N., Harmoush, H., 1996. falta titulo. In: Abe, T., Tsuta, T. (Eds.), Advances in Engineering Plasticity and its Applications. Pergamon, pp. 197–202.

Xue, Z., Vaziri, A., Hutchinson, J., 2008. Material aspects of dynamic neck retardation. Journal of the Mechanics and Physics of Solids 56, 93–113.

Zaera, R., Fernández-Sáez, J., 2006. An implicit consistent algorithm for the integration of thermoviscoplastic constitutive equations in adiabatic conditions and finite deformations. International Journal of Solids and Structures 43, 1594–1612.

Zaera, R., Rodríguez-Martínez, J. A., Vadillo, G., Fernández-Sáez, J., 2014. Dynamic necking in materials with strain induced martensitic transformation. Journal of the Mechanics and Physics of Solids 64, 316–337.

Zhang, C., Guines, D., Leotoing, L., Ragneau, E., 2009. Theoretical and numerical study of strain rate influence on AA5083 formability. Journal of Materials Processing Technology 209, 3849–3858.

Zhang, H., Ravi-Chandar, K., 2006. On the dynamics of necking and fragmentation - I. Real-time and post-mortem observations in Al 6061-O. International Journal of Fracture 142, 183–217.

Zhang, H., Ravi-Chandar, K., 2008. On the dynamics of necking and fragmentation - II. Effect of material properties geometrical constraints and absolute size. International Journal of Fracture 150, 3–36.

Zhou, F., Molinari, J. F., Ramesh, K. T., 2006. An elasto-visco-plastic analysis of ductile expanding ring. Int J Impact Eng 33, 880–891.

Zhu, X., Weinmann, K., Chandra, A., 2001. A unified bifurcation analysis of sheet metal forming limits. ASME Journal of Engineering Materials and Technology 123, 329–333.

Zidane, I., Guines, D., Leotoing, L., Ragneau, E., 2010. Development of an in-plane biaxial test for forming limit curve (FLC) characterization of metallic sheets. Measurement Science and Technology 21, 55701–55711.

Zukas, J. A., Scheffer, D. R., 2000. Practical aspects of numerical simulations of dynamic events: effects of meshing. International Journal of Impact Engineering 24, 925–945.